PHYSICAL REVIEW D **93,** 123522 (2016)

Impacts of biasing schemes in the one-loop integrated perturbation theory

Takahiko Matsubara[*]

Department of Physics, Nagoya University, Chikusa, Nagoya 464-8602, Japan and Kobayashi-Maskawa Institute for the Origin of Particles and the Universe (KMI), Nagoya University, Chikusa, Nagoya 464-8602, Japan

Vincent Desjacques[†]

Département de Physique Théorique and Center for Astroparticle Physics (CAP) Université de Genève, 24 quai Ernest Ansermet, CH-1211 Genève, Switzerland

(Received 22 April 2016; published 22 June 2016)

The impact of biasing schemes on the clustering of tracers of the large-scale structure is analytically studied in the weakly nonlinear regime. For this purpose, we use the one-loop approximation of the integrated perturbation theory together with the renormalized bias functions of various, physically motivated Lagrangian bias schemes. These include the halo, peaks, and excursion set peaks model, for which we derive useful formulas for the evaluation of their renormalized bias functions. The shapes of the power spectra and correlation functions are affected by the different bias models at the level of a few percent on weakly nonlinear scales. These effects are studied quantitatively both in real and redshift space. The amplitude of the scale-dependent bias in the presence of primordial non-Gaussianity also depends on the details of the bias models. If left unaccounted for, these theoretical uncertainties could affect the robustness of the cosmological constraints extracted from galaxy clustering data.

DOI: 10.1103/PhysRevD.93.123522

I. INTRODUCTION

The large-scale structure (LSS) of the universe contains rich information on cosmology. The LSS is mainly probed by the spatial distributions of astronomical objects, such as galaxies, clusters of galaxies, or any other tracer that can be observed in the distant Universe (such as the Lyman-alpha forest, etc.) The spatial distribution of these objects differs from that of the total mass (which includes the mysterious dark matter), while direct predictions from cosmological theories are made for the mass distributions. In fact, except for the lensing shear, essentially all observables of the LSS are biased tracers of the mass distribution.

Although a relation between the spatial distribution of biased tracers and that of the matter is not trivial at small scales owing to the complexity of the physical processes governing star formation, etc., the large-scale clustering of LSS tracers is much less complicated as it is "only" governed by gravity. On very large scales, the biasing is simply given by a linear relation [1,2], and all the complications which arise from the biasing mechanisms are confined to a single variable known as the linear bias factor. In particular, the power spectrum $P_X(k)$ of biased tracers X is linearly related to that of the mass $P_{\rm m}(k)$ through

$$P_X(k) = {b_X}^2 P_{\rm m}(k), \tag{1}$$

where b_X is the linear bias factor of X. The label X represents any kind of biased tracers, i.e. a particular type of galaxies or clusters of galaxies within a certain range of mass for instance. The correlation function, which is the three-dimensional Fourier transform of the power spectrum, satisfies a similar relation, $\xi_X(r) = {b_X}^2 \xi_{\rm m}(r)$.

In redshift surveys, the radial distances to the objects are measured by their redshifts. The observed redshifts are contaminated by the peculiar velocities of the LSS tracers. As a result, clustering patterns in redshift space are distorted along the lines of sight. This effect is known as the redshift-space distortions. In the linear regime, the redshift-space distortions of the power spectrum are analytically given by Kaiser's formula [3],

$$P_X(\boldsymbol{k}) = {b_X}^2 (1 + \beta_X \mu^2)^2 P_{\rm m}(k), \tag{2}$$

where $\mu = \hat{\boldsymbol{z}} \cdot \boldsymbol{k}/|\boldsymbol{k}|$ is the direction cosine between the lines of sight $\hat{\boldsymbol{z}}$ and the wave vector $\boldsymbol{k}$. The variable $\beta_X = f/b_X$, where $f = \ln D/\ln a$ is the linear growth rate, is called the redshift-space distortion parameter. The correlation function in redshift space is given by a Fourier transform of Kaiser's formula [4].

However, the linear theory with linear bias is valid only in the large-scale limit. It is severely violated at small scales where nonlinearities induced by gravitational coupling become important, and exact analytical treatments are extremely difficult. Fortunately, there is an intermediate range of scales between the linear and the highly nonlinear regimes where nonlinearities are weak, so that statistical

[*]taka@kmi.nagoya-u.ac.jp
[†]Vincent.Desjacques@unige.ch

correlators such as the power spectrum and correlation function are amenable to a perturbative treatment (for a review of perturbation theory in LSS, see Ref. [5]).

The traditional perturbation theory predicts weakly nonlinear evolutions of unbiased dark matter in real space. The integrated perturbation theory (iPT) [6,7] is a general framework to predict the weakly nonlinear power spectra and higher-order polyspectra of biased tracers both in real space and in redshift space. This is essential for the analysis of future redshift survey data. Furthermore, the iPT can also include the effect of a primordial non-Gaussianity in the curvature perturbation, which the power spectrum of biased tracers is sensitive to [8]. In principle, any bias model could be incorporated into the iPT. The dependence of the polyspectra on the biasing scheme predicted by the theory is encoded in the so-called *renormalized bias functions*. Hereby, the framework of iPT separates the issue of biasing at small scales from the weakly nonlinear dynamics at larger scales.

The iPT is based on the Lagrangian perturbation theory [9–16], and the renormalized bias functions are directly calculated from the Lagrangian models of bias, in which the bias relations are specified in Lagrangian space. The bias relation is not necessarily a local function of the density in Lagrangian space. In fact, it will involve, e.g., derivatives of the linear density if a peak constraint is present [17,18], as well as the tidal shear if the collapse is not spherical [19–21]. Any kind of bias is represented by a "nonlocal" bias in Lagrangian space, because all the structures in the Universe are formed by a deterministic evolution of the initial density field.

In this work, we investigate the predictions of one-loop iPT for observables such as the power spectrum and correlation function with representative models of Lagrangian bias. The biasing schemes considered in this paper include the halo bias [22,23], peaks model [17,18], and excursion set peaks (ESP) [24,25]. These Lagrangian biasing schemes are physically motivated, and the mass scale is the only parameter left (once the halo mass function or the collapse barrier is known).

The main goal of this paper is to see how differences in the renormalized bias functions predicted by these models are reflected in the weakly nonlinear power spectrum and correlation function. It is not our purpose in this paper to find an accurate model of bias. We are rather interested in assessing the extent to which observed quantities are affected by uncertainties in the biasing. We naively expect that those effects should not be very significant on large scales, because the characteristic formation scales of astrophysical objects are small. Furthermore, the large-scale behavior of the power spectrum and the correlation function is not much affected by small-scale dynamics, except for the scale-independent, linear bias factor. However, scale-dependent corrections predicted, e.g., by a peak constraint can affect the shape of a feature such as the baryon acoustic oscillation [26,27]. These kinds of effects cannot be neglected, should they mimic a signature of fundamental physics detectable in future LSS data or bias cosmological constraints.

Our paper is organized as follows. In Sec. II, the essential equations of the one-loop iPT used in this paper are summarized. In Sec. III, the renormalized bias functions in the bias models considered in paper are derived. In Sec. IV, the resulting predictions of iPT with various biasing schemes are presented for the power spectra and correlation functions in real space and redshift space. The impacts on the scale-dependent bias from primordial non-Gaussianity are indicated. Conclusions are summarized in Sec. V.

II. ONE-LOOP INTEGRATED PERTURBATION THEORY IN A NUTSHELL

In this section, we briefly summarize the formulas of one-loop iPT for the weakly nonlinear power spectra and correlation functions in the presence of bias in general [7].

In this section, we adopt the notation

$$\boldsymbol{k}_{1\cdots n} = \boldsymbol{k}_1 + \cdots + \boldsymbol{k}_n \tag{3}$$

and

$$\int_{\boldsymbol{k}_{1\cdots n}=\boldsymbol{k}} \cdots = \int \frac{d^3k_1}{(2\pi)^3}\cdots\frac{d^3k_n}{(2\pi)^3}(2\pi)^3\delta_{\rm D}^3(\boldsymbol{k}-\boldsymbol{k}_{1\cdots n})\cdots. \tag{4}$$

for brevity. The one-loop power spectrum of biased tracers X is given by the formula

$$\begin{aligned} P_X(\boldsymbol{k}) = {}& [\Gamma_X^{(1)}(\boldsymbol{k})]^2 P_{\rm L}(k) \\ & + \frac{1}{2}\int_{\boldsymbol{k}_{12}=\boldsymbol{k}} [\Gamma_X^{(2)}(\boldsymbol{k}_1,\boldsymbol{k}_2)]^2 P_{\rm L}(k_1)P_{\rm L}(k_2) \\ & + \Gamma_X^{(1)}(\boldsymbol{k})\int_{\boldsymbol{k}_{12}=\boldsymbol{k}} \Gamma_X^{(2)}(\boldsymbol{k}_1,\boldsymbol{k}_2)B_{\rm L}(k,k_1,k_2), \end{aligned} \tag{5}$$

where $P_{\rm L}(k)$ and $B_{\rm L}(k,k_1,k_2)$ are the linear power spectrum and the linear bispectrum, respectively, and $\Gamma_X^{(n)}$ is the nth-order multipoint propagator of biased tracers X. Although the time dependence is omitted in the notation, the functions P_X, $P_{\rm L}$, $B_{\rm L}$, and $\Gamma_X^{(n)}$ depend also on the cosmic time or the redshift of observed objects. In the notation of this paper, the time variable is always omitted in the argument of all the functions for shorthand convenience.

The multipoint propagator of biased tracers can be decomposed into a vertex resummation factor and a normalized propagator as follows,

$$\Gamma_X^{(n)}(\boldsymbol{k}_1,\ldots,\boldsymbol{k}_n) = \Pi(\boldsymbol{k}_{1\cdots n})\hat{\Gamma}_X^{(n)}(\boldsymbol{k}_1,\ldots,\boldsymbol{k}_n), \tag{6}$$

where $\Pi(\boldsymbol{k}) = \langle e^{-i\boldsymbol{k}\cdot\boldsymbol{\Psi}}\rangle$ is the vertex resummation factor and $\boldsymbol{\Psi}$ is a displacement field in the Lagrangian description of cosmological perturbations. The propagators are evaluated with Lagrangian perturbation theory in iPT. The Fourier transform of the displacement field, $\tilde{\boldsymbol{\Psi}}(\boldsymbol{k})$, is expanded by the linear density contrast $\delta_{\rm L}(\boldsymbol{k})$ in Fourier space as

$$\tilde{\boldsymbol{\Psi}}(\boldsymbol{k}) = \sum_{n=1}^{\infty}\frac{i}{n!}\int_{\boldsymbol{k}_{1\cdots n}=\boldsymbol{k}} \boldsymbol{L}^{(n)}(\boldsymbol{k}_1,\ldots,\boldsymbol{k}_n)\delta_{\rm L}(\boldsymbol{k}_1)\cdots\delta_{\rm L}(\boldsymbol{k}_n), \quad (7)$$

which define the Lagrangian kernel functions $\boldsymbol{L}^{(n)}$. The kernel functions are calculated by the Lagrangian perturbation theory [9–12,16]. They are polynomials of the wave vectors which make up their arguments. The Lagrangian kernels in redshift space are obtained by linear transformations of those in real space. For concrete expressions for the Lagrangian kernels in real space and in redshift space, see Refs. [16,28,29].

Up to the one-loop order in Eq. (5), we have

$$\Pi(\boldsymbol{k}) = \exp\left\{-\frac{1}{2}\int\frac{d^3p}{(2\pi)^3}[\boldsymbol{k}\cdot\boldsymbol{L}^{(1)}(\boldsymbol{p})]^2 P_{\rm L}(p)\right\}, \quad (8)$$

$$\begin{aligned}\hat{\Gamma}_X^{(1)}(\boldsymbol{k}) &= c_X^{(1)}(\boldsymbol{k}) + \boldsymbol{k}\cdot\boldsymbol{L}^{(1)}(\boldsymbol{k}) \\ &+ \int\frac{d^3p}{(2\pi)^3}P_{\rm L}(p)\Big\{c_X^{(2)}(\boldsymbol{k},\boldsymbol{p})[\boldsymbol{k}\cdot\boldsymbol{L}^{(1)}(-\boldsymbol{p})] \\ &+ c_X^{(1)}(\boldsymbol{p})[\boldsymbol{k}\cdot\boldsymbol{L}^{(1)}(-\boldsymbol{p})][\boldsymbol{k}\cdot\boldsymbol{L}^{(1)}(\boldsymbol{k})] \\ &+ \frac{1}{2}\boldsymbol{k}\cdot\boldsymbol{L}^{(3)}(\boldsymbol{k},\boldsymbol{p},-\boldsymbol{p}) + c_X^{(1)}(\boldsymbol{p})[\boldsymbol{k}\cdot\boldsymbol{L}^{(2)}(\boldsymbol{k},-\boldsymbol{p})] \\ &+ [\boldsymbol{k}\cdot\boldsymbol{L}^{(1)}(\boldsymbol{p})][\boldsymbol{k}\cdot\boldsymbol{L}^{(2)}(\boldsymbol{k},-\boldsymbol{p})]\Big\} \end{aligned} \quad (9)$$

and

$$\begin{aligned}\hat{\Gamma}_X^{(2)}(\boldsymbol{k}_1,\boldsymbol{k}_2) &= c_X^{(2)}(\boldsymbol{k}_1,\boldsymbol{k}_2) + c_X^{(1)}(\boldsymbol{k}_1)[\boldsymbol{k}\cdot\boldsymbol{L}^{(1)}(\boldsymbol{k}_2)] \\ &+ c_X^{(1)}(\boldsymbol{k}_2)[\boldsymbol{k}\cdot\boldsymbol{L}^{(1)}(\boldsymbol{k}_1)] \\ &+ [\boldsymbol{k}\cdot\boldsymbol{L}^{(1)}(\boldsymbol{k}_1)][\boldsymbol{k}\cdot\boldsymbol{L}^{(1)}(\boldsymbol{k}_2)] + \boldsymbol{k}\cdot\boldsymbol{L}^{(2)}(\boldsymbol{k}_1,\boldsymbol{k}_2), \end{aligned} \quad (10)$$

where $c_X^{(1)}$ and $c_X^{(2)}$ are the renormalized bias functions. The third line of Eq. (9) is usually zero for $c_X^{(1)}(\boldsymbol{p})$ is only a function of the modulus of $\boldsymbol{p}$, $c_X^{(1)}(p)$. The series of renormalized bias functions is generally defined by [30]

$$\begin{aligned}&\left\langle\frac{\delta^n\delta_X^{\rm L}(\boldsymbol{k})}{\delta\delta_{\rm L}(\boldsymbol{k}_1)\cdots\delta\delta_{\rm L}(\boldsymbol{k}_n)}\right\rangle \\ &\quad = (2\pi)^{3-3n}\delta_{\rm D}^3(\boldsymbol{k}-\boldsymbol{k}_{1\cdots n})c_X^{(n)}(\boldsymbol{k}_1,\ldots,\boldsymbol{k}_n), \end{aligned} \quad (11)$$

where $\delta_X^{\rm L}(\boldsymbol{k})$ is the Fourier transform of the density contrast of biased tracers in Lagrangian space, $\delta/\delta\delta_{\rm L}(\boldsymbol{k})$ is the functional derivative with respect to $\delta_{\rm L}$, and $\langle\cdots\rangle$ denotes the statistical average. All the statistical information about spatial biasing is included in the set of renormalized bias functions.

In Lagrangian biasing schemes in general, the number density $n_X^{\rm L}$ of biased tracers in Lagrangian space is modelled as a functional of the linear density field, $n_X^{\rm L} = \mathcal{F}[\delta_{\rm L}]$. The relation is generally given by a functional, instead of a function, because the density of biased tracers at some position is determined by the linear density field not only at the same position but also at other positions as well. We thus have functional derivatives as in Eq. (11).

Once the number density of biased tracers $n_X^{\rm L}$ is modelled as a functional of the linear density field, and the statistical distribution of the linear density field is specified, the renormalized bias functions are obtained from Eq. (11) and $\delta_X^{\rm L} = n_X^{\rm L}/\langle n_X^{\rm L}\rangle - 1$. In order to evaluate the one-loop power spectrum of Eq. (5), only two functions, $c_X^{(1)}(\boldsymbol{k})$ and $c_X^{(2)}(\boldsymbol{k}_1,\boldsymbol{k}_2)$, are required. Some of the angular integrations can be performed analytically, so that Eq. (9) reduces to two- and one-dimensional integrals [7].

In real space, the power spectrum $P_X(k)$ is a function of the modulus of wave vector $k = |\boldsymbol{k}|$ for homogeneous and isotropic random fields. In this case, the correlation function is simply given by

$$\xi_X(r) = \int_0^\infty\frac{k^2dk}{2\pi^2}j_0(kr)P_X(k), \quad (12)$$

where $j_0(z)$ denotes the spherical Bessel function $j_l(z)$ of order zero, $l = 0$. In redshift space, however, the power spectrum has an angular dependence as well. Adopting the distant-observer approximation where all the lines of sight have a common direction, the power spectrum $P_X(k,\mu)$ is a function of the modulus k and direction cosine μ relative to the line of sight. In this case, it is convenient to expand the angular dependence of the power spectrum in Legendre polynomials $\mathsf{P}_l(\mu)$ according to

$$P_X(k,\mu) = \sum_{l=0}^{\infty}p_X^l(k)\mathsf{P}_l(\mu); \quad (13)$$

$$p_X^l(k) = \frac{2l+1}{2}\int_{-1}^{1}d\mu\mathsf{P}_l(\mu)P_X(k,\mu). \quad (14)$$

The same expansion of the correlation function is given by

$$\xi_X(r,\mu) = \sum_{l=0}^{\infty}\xi_X^l(r)\mathsf{P}_l(\mu); \quad (15)$$

$$\xi_X^l(r) = \frac{2l+1}{2}\int_{-1}^{1}d\mu\mathsf{P}_l(\mu)\xi_X(r,\mu). \quad (16)$$

The relation between the multipole coefficients is

$$\xi_X^l(r) = i^{-l}\int_0^\infty \frac{k^2dk}{2\pi^2} j_l(kr)p_X^l(k). \tag{17}$$

Thus, once the power spectrum in redshift space $P_X(k,\mu)$ is calculated by iPT, the multipoles $p_X^l(k)$ and $\xi_X^l(r)$ are evaluated by Eqs. (14) and (17). Analytical integrations of Eq. (14) are also possible [7].

III. RENORMALIZED BIAS FUNCTIONS IN SEMILOCAL MODELS OF BIAS

The concept of renormalized bias functions in the formalism of iPT is applicable to a broad range of generally nonlocal models of bias. However, most of the bias models that have been proposed in recent years fall into a category of, what we call in this paper, semilocal models of bias. In this type of biasing models, the formation sites of LSS tracers depend on the local values of the smoothed mass density field and its spatial derivatives. In this section, we present a general derivation of the renormalized bias functions for a class of semilocal models of Lagrangian bias. To illustrate our method, we compute the renormalized bias functions for a few bias models: the halo, peaks, and ESP models.

A. Semilocal models of Lagrangian bias

In the semilocal models, the number density field $n_X(\boldsymbol{x})$ of observable objects X is described by a function of the smoothed linear density contrast δ_s and its spatial derivatives $\partial_i\delta_s$, $\partial_{ij}\delta_s$, etc. In general, various types of filtering kernels can be simultaneously introduced to accommodate specific variables. For instance, the linear gravitational potential can be included in a straightforward manner by adding a suitable smoothing kernel.

To keep the discussion general, we consider here various smoothing of the linear density contrast,

$$\delta_s(\boldsymbol{x}) = \int \frac{d^3k}{(2\pi)^3}\delta_{\rm L}(\boldsymbol{k})W_s(kR_s)e^{i\boldsymbol{k}\cdot\boldsymbol{x}}, \tag{18}$$

where the index s refers to the types of smoothing kernel; $\delta_{\rm L}$ is a linear density contrast in Fourier space; and W_s and R_s are, respectively, a smoothing function and a smoothing radius for each type s of the smoothing kernel. Popular kernels include the top-hat ($s = {\rm T}$) and Gaussian ($s = {\rm G}$) window functions,

$$W_{\rm T}(x) = 3j_1(x)/x, \qquad W_{\rm G}(x) = e^{-x^2/2}. \tag{19}$$

The linear gravitational potential $\phi_{\rm L}$ can also be expressed in the form of Eq. (18) with a smoothing kernel $W_\phi(x) = -1/x^2$ and smoothing radius $R_\phi = a^{-1}(4\pi G\bar{\rho})^{-1/2}$. In this case, we have $s = \phi$ and $\delta_\phi = \phi_{\rm L}$. Another example is the effective window function $W_{\rm eff}(x) = W_{\rm T}(x)W_{\rm G}(f_{\rm eff}^{1/2}x/5)$ recently proposed by Ref. [31] to model Lagrangian halos. Here, $f_{\rm eff}$ is a free parameter that must be calibrated with simulations. This effective window function furnishes a good fit to the small-scale, scale-dependent Lagrangian halo bias measured from numerical simulations.

While Eq. (18) can incorporate many different smoothing functions such as, e.g., $s = \phi$, we specifically consider biasing models that depend on the spatial derivatives of the smoothed field up to second order, $\partial_i\delta_s$ and $\partial_{ij}\delta_s$, in addition to the field values themselves, δ_s. It is convenient to introduce the spectral moments $\sigma_{s0} = \langle(\delta_s)^2\rangle^{1/2}$, $\sigma_{s1} = \langle\boldsymbol{\nabla}\delta_s\cdot\boldsymbol{\nabla}\delta_s\rangle^{1/2}$, and $\sigma_{s2} = \langle(\boldsymbol{\nabla}\cdot\boldsymbol{\nabla}\delta_s)^2\rangle^{1/2}$ so as to normalize the linear density fields:

$$\nu_s(\boldsymbol{x}) = \frac{\delta_s(\boldsymbol{x})}{\sigma_{s0}}, \quad \eta_{si}(\boldsymbol{x}) = \frac{\partial_i\delta_s(\boldsymbol{x})}{\sigma_{s1}}, \quad \zeta_{sij}(\boldsymbol{x}) = \frac{\partial_i\partial_j\delta_s(\boldsymbol{x})}{\sigma_{s2}}. \tag{20}$$

The spectral parameters are integrals of the linear power spectrum $P_{\rm L}(k)$,

$$\sigma_{sj}{}^2 = \int \frac{k^2dk}{2\pi^2}k^{2j}P_{\rm L}(k)[W_s(kR_s)]^2. \tag{21}$$

The number density field $n_X(\boldsymbol{x})$ of biased objects is assumed to be a multivariate function of ν_s, η_{si}, and ζ_{sij}, where the filtering kernels can be $s = {\rm T}, {\rm G}, {\rm eff}, \ldots$, and the spatial indices run over $i = 1, 2, 3$ and $ij = 11, 22, 33, 12, 23, 13$. These linear field variables are denoted by y_α, where the index α indicates one of the above field variables, such as $\nu_{\rm T}$, $\eta_{\rm G2}$, $\zeta_{\rm G13}$, etc.

The Fourier transform of the variables $y_\alpha(\boldsymbol{x})$ is of the form

$$\tilde{y}_\alpha(\boldsymbol{k}) = U_\alpha(\boldsymbol{k})\delta_{\rm L}(\boldsymbol{k}), \tag{22}$$

where the functions $U_\alpha(\boldsymbol{k})$ corresponding to the variables in Eq. (20) are given by $W_s(\boldsymbol{k})/\sigma_{s0}$, $ik_iW_s(\boldsymbol{k})/\sigma_{s1}$, and $-k_ik_jW_s(\boldsymbol{k})/\sigma_{s2}$, respectively. The renormalized bias functions of iPT are given by [6]

$$c_X^{(n)}(\boldsymbol{k}_1,\ldots,\boldsymbol{k}_n) = \frac{1}{\bar{n}_X}\sum_{\alpha_1,\ldots,\alpha_n}\left\langle\frac{\partial^n n_X}{\partial y_{\alpha_1}\cdots\partial y_{\alpha_n}}\right\rangle \times U_{\alpha_1}(\boldsymbol{k}_1)\cdots U_{\alpha_n}(\boldsymbol{k}_n). \tag{23}$$

Here, $\bar{n}_X = \langle n_X\rangle$ is the mean number density of objects X. It is convenient to define a differential operator

$$\mathcal{D}(\boldsymbol{k}) \equiv \sum_\alpha U_\alpha(\boldsymbol{k})\frac{\partial}{\partial y_\alpha} = \sum_s W_s(kR_s)\left[\frac{1}{\sigma_{s0}}\frac{\partial}{\partial\nu_s} + \frac{i}{\sigma_{s1}}\mathcal{D}_\eta^s(\boldsymbol{k}) - \frac{1}{\sigma_{s2}}\mathcal{D}_\zeta^s(\boldsymbol{k})\right], \tag{24}$$

where

$$\mathcal{D}^s_\eta(\boldsymbol{k}) = \sum_i k_i \frac{\partial}{\partial \eta_{si}}, \qquad \mathcal{D}^s_\zeta(\boldsymbol{k}) = \sum_{i\le j} k_i k_j \frac{\partial}{\partial \zeta_{sij}}. \tag{25}$$

Although the set of variables ζ_{sij} is a symmetric tensor and has six independent degrees of freedom, it is useful to introduce a set of redundant variables,

$$\xi_{sij} \equiv \begin{cases} \zeta_{sij} & (i \le j) \\ \zeta_{sji} & (i > j) \end{cases}. \tag{26}$$

Any function of ζ_{sij} $(i \le j)$ can be considered as a function of ξ_{sij}. The differentiation with respect to independent variables ζ_{sij} is given by

$$\frac{\partial}{\partial \zeta_{sij}} = \begin{cases} \frac{\partial}{\partial \xi_{sii}} & (i = j) \\ \frac{\partial}{\partial \xi_{sij}} + \frac{\partial}{\partial \xi_{sji}} & (i < j) \end{cases}, \tag{27}$$

when it acts on an explicit function of ξ_{sij}. With the variables ξ_{sij}, the differential operator $\mathcal{D}^s_\zeta(\boldsymbol{k})$ in Eq. (25) reduces to

$$\mathcal{D}^s_\zeta(\boldsymbol{k}) = \sum_{i,j} k_i k_j \frac{\partial}{\partial \xi_{sij}}. \tag{28}$$

Using the differential operator $\mathcal{D}(\boldsymbol{k})$, Eq. (23) reduces to

$$\begin{aligned} c^{(n)}_X(\boldsymbol{k}_1, \ldots, \boldsymbol{k}_n) &= \frac{1}{\bar{n}_X} \langle \mathcal{D}(\boldsymbol{k}_1) \cdots \mathcal{D}(\boldsymbol{k}_n) n_X \rangle \\ &= \frac{(-1)^n}{\bar{n}_X} \int d^N y n_X(\boldsymbol{y}) \mathcal{D}(\boldsymbol{k}_1) \cdots \mathcal{D}(\boldsymbol{k}_n) \mathcal{P}(\boldsymbol{y}), \end{aligned} \tag{29}$$

where $\mathcal{P}(\boldsymbol{y})$ is the joint probability distribution function and N is the dimension of y_α. Integrations by parts are applied in the second line. The mean number density is given by

$$\bar{n}_X = \langle n_X \rangle = \int d^N y n_X(\boldsymbol{y}) \mathcal{P}(\boldsymbol{y}). \tag{30}$$

For a given model of bias, the functions $n_X(\boldsymbol{y})$ and $U_\alpha(\boldsymbol{k})$ are specified, and the renormalized bias functions are calculated by Eqs. (29) and (30). The joint probability distribution function $\mathcal{P}(\boldsymbol{y})$ is determined by the statistics of the initial density field $\delta_{\rm L}$.

Equations (29) and (30) are also applicable in the presence of initial non-Gaussianity. When the initial density field is random Gaussian, $\mathcal{P}$ is a multivariate Gaussian distribution function. In this case, the covariance matrix of the set of variables $\{y_\alpha\}$,

$$\mathcal{M}_{\alpha\beta} = \langle y_\alpha y_\beta \rangle = \int \frac{d^3k}{(2\pi)^3} U^*_\alpha(\boldsymbol{k}) U_\beta(\boldsymbol{k}) P_{\rm L}(k), \tag{31}$$

completely determines the distribution function as

$$\mathcal{P}(\boldsymbol{y}) = \frac{1}{\sqrt{(2\pi)^N \det \mathcal{M}}} \exp\left(-\frac{1}{2} \boldsymbol{y}^{\rm T} \mathcal{M}^{-1} \boldsymbol{y}\right). \tag{32}$$

Generalization of the following analysis in the presence of initial non-Gaussianity is fairly straightforward by applying the multivariate Gram-Charlier expansion of the distribution function [32–34].

B. Simple halo model

The renormalized bias functions in the halo model of bias are derived in Ref. [30]. We summarize the results in this subsection. In the halo model, the smoothing radius R is associated with a mass scale M by a relation,

$$M = \frac{4\pi \bar{\rho}_0}{3} R^3, \tag{33}$$

where $\bar{\rho}_0$ is the mean matter density at the present time. The above relation is equivalently represented by

$$R = \left(\frac{M}{1.163 \times 10^{12} h^{-1} M_\odot \Omega_{\rm m0}}\right)^{1/3} h^{-1}\ {\rm Mpc}, \tag{34}$$

where $M_\odot = 1.989 \times 10^{30}$ kg is the solar mass, $\Omega_{\rm m0}$ is the density parameter of the present universe, and $h = H_0/(100\ {\rm km\,s^{-1}\,Mpc^{-1}})$ is the dimensionless Hubble parameter.

The mass element at a Lagrangian position $\boldsymbol{x}$ is assumed to be contained in a halo of mass larger than M, if the value of linear density contrast δ_M smoothed by the mass scale M exceeds a critical value $\delta_{\rm c}$. The critical value is usually taken to be $\delta_{\rm c} = 3(3\pi/2)^{2/3}/5 \simeq 1.686$, which follows from the spherical collapse calculation. The localized differential number density of halos at a Lagrangian position $\boldsymbol{x}$ is given by [30]

$$n(\boldsymbol{x}, M) = -\frac{2\bar{\rho}_0}{M} \frac{\partial}{\partial M} \Theta[\delta_M(\boldsymbol{x}) - \delta_{\rm c}], \tag{35}$$

where $n(\boldsymbol{x}, M)$ is the differential mass function of halos and $\Theta(x)$ is the step function. This model is a generalization of the Press-Schechter (PS) formalism [35]. In fact, on taking the spatial average of the above equation, the number density of halos $n(M)$ in the original PS formalism is recovered.

When the initial condition is Gaussian, and the smoothed mass density contrast $\delta_M(\boldsymbol{x})$ is a Gaussian field, the spatial average of the step function $\langle \Theta(\delta_M(\boldsymbol{x}) - \delta_{\rm c}) \rangle$ is given by the complementary error function. In this case, the global (spatially averaged) mass function has the form

$$n(M)dM = \frac{\bar{\rho}_0}{M} f(\nu) \frac{d\nu}{\nu}, \tag{36}$$

where $\nu = \delta_c/\sigma_M$, $\sigma_M = \langle (\delta_M)^2 \rangle^{1/2}$ are functions of mass M and $f(\nu) = (2/\pi)^{1/2} \nu e^{-\nu^2/2}$. The function $f(\nu)$ is called the "multiplicity function" [Note that another convention defines $f(\nu)$ as $n(M)dM = (\bar{\rho}_0/M) f(\nu) d\nu$].

While the mass function of dark matter halos identified in N-body simulations broadly agrees with the PS prediction, the agreement is far from perfect. Recent studies have shown that using multiplicity functions different from the PS mass function provides better models for halo statistics. One of the simplest models is given by a Sheth-Tormen mass function [36], for which the multiplicity function reads

$$f(\nu) = A(p) \sqrt{\frac{2}{\pi}} \left[1 + \frac{1}{(q\nu^2)^p} \right] \sqrt{q} \nu e^{-q\nu^2/2}, \tag{37}$$

where $p = 0.3$, $q = 0.707$, and $A(p) = [1 + \pi^{-1/2} 2^{-p} \Gamma(1/2 - p)]^{-1}$ is a normalization factor.

When the mass function is changed from the PS one, Eq. (35) should be simultaneously changed in order to be compatible with Eq. (36). This can be achieved by substituting the step function $\Theta(\delta_M - \delta_c)$ with an auxiliary function $\Xi(\delta_M - \delta_c, \sigma_M)$. This function should explicitly depend on the mass M through σ_M. Otherwise, if the mass dependence is only implicit through the smoothing kernel of δ_M, the resulting mass function is only compatible with the PS mass function. More details on the relation between the multiplicity function and the auxiliary function is discussed in Appendix A.

The relation between the multiplicity function $f(\nu)$ and the new function Ξ is given by

$$\langle \Xi(\delta_M - \delta_c, \sigma_M) \rangle = \frac{1}{2} \int_\nu^\infty \frac{f(\nu)}{\nu} d\nu, \tag{38}$$

and the local mass function is given by

$$\begin{aligned} n(\boldsymbol{x}, M) &= -\frac{2\bar{\rho}_0}{M} \frac{\partial}{\partial M} \Xi[\delta_M(\boldsymbol{x}) - \delta_c, \sigma_M] \\ &= \frac{2\bar{\rho}_0}{M} \left\{ \frac{\partial \delta_M(\boldsymbol{x})}{\partial M} \frac{\partial}{\partial \delta_c} \Xi[\delta_M(\boldsymbol{x}) - \delta_c, \sigma_M] \right. \\ &\quad \left. - \frac{d\sigma_M}{dM} \frac{\partial}{\partial \sigma_M} \Xi[\delta_M(\boldsymbol{x}) - \delta_c, \sigma_M] \right\}. \end{aligned} \tag{39}$$

The model of Eq. (39) for the number density field depends on the linear density field through two variables, $\delta_M(\boldsymbol{x})$ and $\partial \delta_M(\boldsymbol{x})/\partial M$, which corresponds to the variables y_α in Sec. III A. The window functions for these variables $U_\alpha(\boldsymbol{k})$ are given by $W(kR)$ and $\partial W(kR)/\partial M$, respectively, where R and M are related by Eq. (33) or (34). The renormalized bias functions in this model are derived by Eqs. (23) and (39). The unknown function Ξ can be removed from the resulting expressions thanks to the relation of Eq. (38). Closed forms for all the renormalized bias functions are derived in Ref. [30]. (In the notation of Ref. [30], the dependence of σ_M in the function Ξ is implicit, but it is actually assumed.) The results are given by

$$\begin{aligned} c_X^{(n)}(\boldsymbol{k}_1, \ldots, \boldsymbol{k}_n) &= b_n^{\mathrm{L}} W(k_1 R) \cdots W(k_n R) \\ &\quad + \frac{A_{n-1}(M)}{{\delta_c}^n} \frac{d}{d \ln \sigma_M} [W(k_1 R) \cdots W(k_n R)], \end{aligned} \tag{40}$$

where

$$b_n^{\mathrm{L}}(M) \equiv \left(-\frac{1}{\sigma_M} \right)^n \frac{f^{(n)}(\nu)}{f(\nu)}, \tag{41}$$

$$A_n(M) \equiv \sum_{m=0}^{n} \frac{n!}{m!} {\delta_c}^m b_m^{\mathrm{L}}(M). \tag{42}$$

In this paper, we need only the first two functions, $c_X^{(1)}$ and $c_X^{(2)}$, which are explicitly given by

$$c_X^{(1)}(k) = b_1^{\mathrm{L}} W(kR) + \frac{1}{\delta_c} \frac{dW(kR)}{d \ln \sigma_M}, \tag{43}$$

$$\begin{aligned} c_X^{(2)}(\boldsymbol{k}_1, \boldsymbol{k}_2) &= b_2^{\mathrm{L}} W(k_1 R) W(k_2 R) \\ &\quad + \frac{1 + \delta_c b_1^{\mathrm{L}}}{{\delta_c}^2} \frac{d[W(k_1 R) W(k_2 R)]}{d \ln \sigma_M}. \end{aligned} \tag{44}$$

C. Peaks model

In the peaks model, the formation sites of dark matter halos are identified with density peaks in Lagrangian space. The peaks are described by field values with up to second derivatives of a smoothed density field, ν_s, η_{si}, and ζ_{sij}. While the choice of smoothing kernel s is arbitrary (so long as the convergence of the spectral moments is ensured), the Gaussian kernel ($s = \mathrm{G}$) is frequently adopted. In the peaks model, only a single kind of smoothing kernel is involved. Therefore, we omit the subscript s in this subsection below and use notations like ν, η_i, ζ_{ij}, σ_0, σ_1, σ_2, etc.

1. Derivation of renormalized bias functions in the peaks model

The differential number density of discrete peaks with a peak height ν_c is given by [17]

$$n_{\mathrm{pk}} = \frac{3^{3/2}}{{R_*}^3} \delta_{\mathrm{D}}(\nu - \nu_c) \delta_{\mathrm{D}}^3(\boldsymbol{\eta}) \Theta(\lambda_3) |\det \boldsymbol{\zeta}|, \tag{45}$$

where $R_* = \sqrt{3}\sigma_1/\sigma_2$ is a characteristic radius and λ_3 is the smallest eigenvalue of the 3×3 matrix $(-\zeta_{ij})$. The number

density of peaks with peak height between ν_c and $\nu_c + d\nu_c$ is given by $n_{pk} d\nu_c$.

The variables (y_α) consists of ten variables, $(\nu, \eta_i, \zeta_{ij})$ with $1 \le i \le j \le 3$, and the corresponding kernels (U_α) are $[W(kR)/\sigma_0, ik_iW(kR)/\sigma_1, -k_ik_jW(kR)/\sigma_2]$.

When the linear density field δ_L is statistically isotropic, the joint probability distribution function $\mathcal{P}(\boldsymbol{y})$ only depends on rotationally invariant quantities [32,33,37]. Using the redundant variables ξ_{ij} defined in Eq. (26), these are

$$\eta^2 \equiv \boldsymbol{\eta}\cdot\boldsymbol{\eta}, \quad J_1 \equiv -\xi_{ii}, \quad J_2 \equiv \frac{3}{2}\tilde{\xi}_{ij}\tilde{\xi}_{ji}, \quad J_3 = \frac{9}{2}\tilde{\xi}_{ij}\tilde{\xi}_{jk}\tilde{\xi}_{ki}, \tag{46}$$

where repeated indices are summed over, and

$$\tilde{\xi}_{ij} \equiv \xi_{ij} + \frac{1}{3}\delta_{ij}J_1, \tag{47}$$

is the traceless part of ξ_{ij}. Covariances among the field variables are given by [17]

$$\langle \nu^2 \rangle = 1, \quad \langle \nu\eta_i \rangle = 0, \quad \langle \nu\xi_{ij} \rangle = -\frac{\gamma}{3}\delta_{ij}, \quad \langle \eta_i\eta_j \rangle = \frac{1}{3}\delta_{ij}, \tag{48}$$

$$\langle \eta_i\xi_{jk} \rangle = 0, \quad \langle \xi_{ij}\xi_{kl} \rangle = \frac{1}{15}(\delta_{ij}\delta_{kl} + \delta_{ik}\delta_{jl} + \delta_{il}\delta_{jk}), \tag{49}$$

where

$$\gamma \equiv \frac{{\sigma_1}^2}{\sigma_0\sigma_2} \tag{50}$$

characterizes the broadband shape of the smoothed linear power spectrum. Adopting the above covariances, the multivariate distribution function of Eq. (32) reduces to [17,18,32,33,37,38]

$$\mathcal{P}(\boldsymbol{y}) \propto \exp\left[-\frac{\nu^2 + {J_1}^2 - 2\gamma\nu J_1}{2(1-\gamma^2)} - \frac{3}{2}\eta^2 - \frac{5}{2}J_2\right] \tag{51}$$

up to a normalization constant, which is irrelevant for our applications in the following. The distribution function above is still for linear variables $\boldsymbol{y}$, and not for rotationally invariant variables.

Since the distribution function $\mathcal{P}(\boldsymbol{y})$ depends only on four rotationally invariant variables ν, J_1, η^2, and J_2, the first-order derivatives are given by

$$\frac{\partial}{\partial\eta_i}\mathcal{P} = 2\eta_i\frac{\partial}{\partial(\eta^2)}\mathcal{P}, \quad \frac{\partial}{\partial\xi_{ij}}\mathcal{P} = \left[-\delta_{ij}\frac{\partial}{\partial J_1} + 3\tilde{\xi}_{ij}\frac{\partial}{\partial J_2}\right]\mathcal{P}, \tag{52}$$

for which the relations

$$\frac{\partial(\eta^2)}{\partial\eta_i} = 2\eta_i, \qquad \frac{\partial J_1}{\partial\xi_{ij}} = -\delta_{ij}, \qquad \frac{\partial J_2}{\partial\xi_{ij}} = 3\tilde{\xi}_{ij} \tag{53}$$

are used. Further differentiating the above equations, we have

$$\frac{\partial^2}{\partial\eta_i\partial\eta_j}\mathcal{P} = \left[2\delta_{ij}\frac{\partial}{\partial(\eta^2)} + 4\eta_i\eta_j\frac{\partial^2}{\partial(\eta^2)^2}\right]\mathcal{P}, \tag{54}$$

$$\frac{\partial^2}{\partial\xi_{ij}\partial\xi_{kl}}\mathcal{P} = \left[\delta_{ij}\delta_{kl}\frac{\partial^2}{\partial {J_1}^2} - 3(\delta_{ij}\tilde{\xi}_{kl} + \delta_{kl}\tilde{\xi}_{ij})\frac{\partial^2}{\partial J_1\partial J_2} + 9\tilde{\xi}_{ij}\tilde{\xi}_{kl}\frac{\partial^2}{\partial {J_2}^2} + (3\delta_{ik}\delta_{jl} - \delta_{ij}\delta_{kl})\frac{\partial}{\partial J_2}\right]\mathcal{P}, \tag{55}$$

where a relation $\partial\tilde{\xi}_{kl}/\partial\xi_{ij} = \delta_{ik}\delta_{jl} - \delta_{ij}\delta_{kl}/3$ is used.

The number density of peaks $n_{pk}(\boldsymbol{y})$ and the distribution function $\mathcal{P}(\boldsymbol{y})$ both depend only on rotationally invariant variables. Thus, the differential operators $\mathcal{D}(\boldsymbol{k}_1)\cdots\mathcal{D}(\boldsymbol{k}_n)$ in Eq. (29) can be replaced by those averaged over the rotation of coordinates, $\langle\cdots\rangle_\Omega$. For that purpose, we have

$$\langle\eta_i\rangle_\Omega = 0, \qquad \langle\eta_i\eta_j\rangle_\Omega = \frac{1}{3}\delta_{ij}\eta^2, \qquad \langle\tilde{\xi}_{ij}\rangle_\Omega = 0, \tag{56}$$

$$\langle\tilde{\xi}_{ij}\tilde{\xi}_{kl}\rangle_\Omega = \frac{1}{15}\left(\delta_{ik}\delta_{jl} + \delta_{il}\delta_{jk} - \frac{2}{3}\delta_{ij}\delta_{kl}\right)J_2, \tag{57}$$

and so forth.

Combining Eqs. (24), (25), (28), and (52)–(57), we have

$$\langle\mathcal{D}(\boldsymbol{k})\rangle_\Omega\mathcal{P} = W(kR)\left(\frac{1}{\sigma_0}\frac{\partial}{\partial\nu} + \frac{k^2}{\sigma_2}\frac{\partial}{\partial J_1}\right)\mathcal{P}, \tag{58}$$

$$\begin{aligned}\langle\mathcal{D}(\boldsymbol{k}_1)\mathcal{D}(\boldsymbol{k}_2)\rangle_\Omega\mathcal{P} &= W(k_1R)W(k_2R)\\ &\times\left\{\left(\frac{1}{\sigma_0}\frac{\partial}{\partial\nu} + \frac{{k_1}^2}{\sigma_2}\frac{\partial}{\partial J_1}\right)\left(\frac{1}{\sigma_0}\frac{\partial}{\partial\nu} + \frac{{k_2}^2}{\sigma_2}\frac{\partial}{\partial J_1}\right)\right.\\ &-\frac{2(\boldsymbol{k}_1\cdot\boldsymbol{k}_2)}{{\sigma_1}^2}\left[1 + \frac{2}{3}\eta^2\frac{\partial}{\partial(\eta^2)}\right]\frac{\partial}{\partial(\eta^2)}\\ &\left.+\frac{3(\boldsymbol{k}_1\cdot\boldsymbol{k}_2)^2 - {k_1}^2{k_2}^2}{{\sigma_2}^2}\left[1 + \frac{2}{5}\zeta^2\frac{\partial}{\partial J_2}\right]\frac{\partial}{\partial J_2}\right\}\mathcal{P}.\end{aligned} \tag{59}$$

Derivatives with respect to variables ν and J_1 in Eqs. (58) and (59) can be represented by bivariate Hermite polynomials [38],

$$H_{ij}(\nu, J_1) \equiv \frac{(-1)^{i+j}}{\mathcal{N}(\nu, J_1)}\left(\frac{\partial}{\partial\nu}\right)^i\left(\frac{\partial}{\partial J_1}\right)^j\mathcal{N}(\nu, J_1), \tag{60}$$

where

$$\mathcal{N}(\nu, J_1) \equiv \frac{1}{2\pi\sqrt{1-\gamma^2}} \exp\left[-\frac{\nu^2 + {J_1}^2 - 2\gamma\nu J_1}{2(1-\gamma^2)}\right] \tag{61}$$

is the bivariate normal distribution function. Derivatives with respect to variables η^2 and J_2 are straightforwardly obtained as

$$\left[1 + \frac{2}{3}\eta^2 \frac{\partial}{\partial(\eta^2)}\right] \frac{\partial}{\partial(\eta^2)} e^{-3\eta^2/2} = \frac{3}{2}(\eta^2 - 1)e^{-3\eta^2/2} = -L_1^{(1/2)}\left(\frac{3}{2}\eta^2\right) e^{-3\eta^2/2}, \tag{62}$$

$$\left[1 + \frac{2}{5}J_2 \frac{\partial}{\partial J_2}\right] \frac{\partial}{\partial J_2} e^{-5J_2/2} = \frac{5}{2}(J_2 - 1)e^{-5J_2/2} = -L_1^{(3/2)}\left(\frac{5}{2}J_2\right) e^{-5J_2/2}, \tag{63}$$

where

$$L_n^{(\alpha)}(x) = \frac{x^{-\alpha}e^x}{n!}\frac{d^n}{dx^n}(x^{n+\alpha}e^{-x}) \tag{64}$$

are the generalized Laguerre polynomials.

Substituting Eqs. (58) and (59) into the integrand of Eq. (29), we obtain

$$c_X^{(1)}(k) = (b_{10} + b_{01}k^2)W(kR), \tag{65}$$

$$c_X^{(2)}(\boldsymbol{k}_1, \boldsymbol{k}_2) = \Big\{ b_{20} + b_{11}({k_1}^2 + {k_2}^2) + b_{02}{k_1}^2{k_2}^2 - 2\chi_1(\boldsymbol{k}_1 \cdot \boldsymbol{k}_2) + \omega_{10}[3(\boldsymbol{k}_1 \cdot \boldsymbol{k}_2)^2 - {k_1}^2{k_2}^2] \Big\} W(k_1R)W(k_2R), \tag{66}$$

where

$$b_{ij} \equiv \frac{1}{{\sigma_0}^i {\sigma_2}^j \bar{n}_{\rm pk}} \int d^{10}y n_{\rm pk} H_{ij}(\nu, J_1)\mathcal{P}, \tag{67}$$

$$\chi_k \equiv \frac{(-1)^k}{{\sigma_1}^{2k}\bar{n}_{\rm pk}} \int d^{10}y n_{\rm pk} L_k^{(1/2)}\left(\frac{3}{2}\eta^2\right)\mathcal{P}, \tag{68}$$

$$\omega_{l0} \equiv \frac{(-1)^l}{{\sigma_2}^{2l}\bar{n}_{\rm pk}} \int d^{10}y n_{\rm pk} L_l^{(3/2)}\left(\frac{5}{2}J_2\right)\mathcal{P}. \tag{69}$$

The higher-order renormalized bias functions $c_X^{(n)}$ can be similarly obtained by further differentiating Eqs. (54) and (55) and following similar procedures as above.

The above results have exactly the same form as the peak bias functions, which have been derived in Refs. [18,38]. These authors generalized the peak-background split and argued that the peak bias factors indeed are the ensemble average of orthogonal polynomials. However, they did not explicitly demonstrate that their generalized polynomial expansion holds beyond second order. In Appendix B, we briefly sketch how this could be done and emphasize the connection between the peak approach and the iPT.

Note that, as the peak constraint $n_{\rm pk}$ has a factor $\delta_{\rm D}^3(\boldsymbol{\eta})$, only the constant term of the generalized Laguerre polynomials $L_n^{(\alpha)}(0) = \Gamma(n+\alpha+1)/[\Gamma(n+1)\Gamma(\alpha+1)]$ appears. Therefore, Eq. (68) reduces to

$$\chi_k = \frac{(2k+1)!!}{2^k k!}\frac{(-1)^k}{{\sigma_1}^{2k}}. \tag{70}$$

The integrals Eqs. (67), (68), and (69) appear up to second order, i.e., in the functions $c_X^{(1)}$ and $c_X^{(2)}$. Note, however, that the bias coefficients will generically take the form [33]

$$\int d^{10}y n_{\rm pk} H_{ij}(\nu, J_1) L_k^{(1/2)}\left(\frac{3}{2}\eta^2\right) F_{lm}(5J_2, J_3)\mathcal{P}, \tag{71}$$

in the renormalized bias functions $c_X^{(n)}$ with $n \geq 3$ [18], where

$$F_{lm}(5J_2, J_3) \equiv (-1)^l \sqrt{\frac{\Gamma(5/2)}{2^{3m}\Gamma(3m+5/2)}} \times L_l^{(3m+3/2)}\left(\frac{5}{2}J_2\right) P_m\left(\frac{J_3}{{J_2}^{3/2}}\right) \tag{72}$$

are polynomials of J_2 and J_3, orthogonalized with the Gram-Schmidt procedure and $P_m(x)$ are Legendre polynomials. The appearance of $P_m(x)$ reflects the fact that J_3 is an "angular" variable. This is the reason why we adopt the notation χ_k and ω_{l0} of Ref. [18]. We refer the reader to this work for more details.

2. Bias coefficients of peaks model

Even though the bias coefficients b_{ij}, χ_k, and ω_{l0} are explicitly defined as ten-dimensional integrals, they can be reduced to one-dimensional integrals at most. Explicit formulas of the coefficients are derived below.

To begin with, we define a set of integrals:

$$A_n^{\rm pk}(\nu_{\rm c}) \equiv \frac{1}{\bar{n}_{\rm pk}} \int d^{10}y n_{\rm pk} {J_1}^n \mathcal{P}, \tag{73}$$

$$B_n^{\rm pk}(\nu_{\rm c}) \equiv \frac{1}{\bar{n}_{\rm pk}} \int d^{10}y n_{\rm pk} J_2{}^n \mathcal{P}. \tag{74}$$

All the bias coefficients defined in Eqs. (67) and (68) can be represented by the above functions $A_n^{\rm pk}$ and $B_n^{\rm pk}$ of Eqs. (73) and (74), because H_{ij} and $L_n^{(\alpha)}$ are just polynomials of their arguments, and peak constraints in $n_{\rm pk}$ contain delta functions as $\delta_{\rm D}(\nu-\nu_{\rm c})\delta_{\rm D}^3(\boldsymbol{\eta})$. Defining invariant variables

$$x=\lambda_1+\lambda_2+\lambda_3, \quad y=\frac{1}{2}(\lambda_1-\lambda_2), \quad z=\frac{1}{2}(\lambda_1-2\lambda_2+\lambda_3), \tag{75}$$

where λ_1, λ_2, λ_3 are eigenvalues of $-\zeta_{ij}$ with a descending order ($\lambda_1 \geq \lambda_2 \geq \lambda_3$), the peak number density of Eq. (45) reduces to [17]

$$n_{\rm pk} = \frac{2}{\sqrt{3}R_*{}^3}\delta_{\rm D}(\nu-\nu_{\rm c})\delta_{\rm D}^3(\boldsymbol{\eta})(x-2z)[(x+z)^2-(3y)^2] \times \Theta(y-z)\Theta(y+z)\Theta(x-3y+z). \tag{76}$$

Other variables in Eqs. (73) and (74) correspond to $J_1 = x$, $J_2 = 3y^2+z^2$. Following similar calculations in Ref. [17], and defining a function

$$F(x,y,z) \equiv (x-2z)[(x+z)^2-(3y)^2]y(y^2-z^2), \tag{77}$$

Eqs. (73) and (74) reduce to

$$A_n^{\rm pk}(\nu_{\rm c}) = \frac{\int_0^\infty dx x^n f_0(x)\mathcal{N}(\nu_{\rm c},x)}{\int_0^\infty dx f_0(x)\mathcal{N}(\nu_{\rm c},x)}, \tag{78}$$

$$B_n^{\rm pk}(\nu_{\rm c}) = \frac{\int_0^\infty dx f_n(x)\mathcal{N}(\nu_{\rm c},x)}{\int_0^\infty dx f_0(x)\mathcal{N}(\nu_{\rm c},x)}, \tag{79}$$

where the function $\mathcal{N}$ is given by Eq. (61) and

$$f_n(x) \equiv \frac{3^2 5^{5/2}}{\sqrt{2\pi}}\left(\int_0^{x/4} dy \int_{-y}^{y} dz + \int_{x/4}^{x/2} dy \int_{3y-x}^{y} dz\right) \times (3y^2+z^2)^n F(x,y,z) e^{-5(3y^2+z^2)/2}. \tag{80}$$

The function $f_0(x)$ is identical to the function $f(x)$ defined by Eq. (A.15) of Ref. [17]:

$$f_0(x) = \frac{x}{2}(x^2-3)\left[{\rm erf}\left(\frac{1}{2}\sqrt{\frac{5}{2}}x\right)+{\rm erf}\left(\sqrt{\frac{5}{2}}x\right)\right] + \sqrt{\frac{2}{5\pi}}\left[\left(\frac{x^2}{2}-\frac{8}{5}\right)e^{-5x^2/2}+\left(\frac{31}{4}x^2+\frac{8}{5}\right)e^{-5x^2/8}\right]. \tag{81}$$

With the same consideration in Ref. [38], the analytically closed form of Eq. (80) is derived from $f_0(x)$ as

$$f_n(x) = \left(-\frac{2}{5}\frac{\partial}{\partial\alpha}\right)^n\left[\frac{f_0(\alpha^{1/2}x)}{\alpha^4}\right]\Bigg|_{\alpha=1}. \tag{82}$$

For example, the explicit form of $n=1$ is given by

$$f_1(x) = \frac{x}{2}\left(x^2-\frac{21}{5}\right)\left[{\rm erf}\left(\frac{1}{2}\sqrt{\frac{5}{2}}x\right)+{\rm erf}\left(\sqrt{\frac{5}{2}}x\right)\right] + \sqrt{\frac{2}{5\pi}}\left[\left(\frac{x^2}{2}-\frac{64}{25}\right)e^{-5x^2/2} + \left(\frac{27}{16}x^4+\frac{209}{20}x^2+\frac{64}{25}\right)e^{-5x^2/8}\right]. \tag{83}$$

Thus, the originally ten-dimensional integrals of Eqs. (73) and (74) reduce to just one-dimensional ones of Eqs. (78) and (79), for which numerically evaluations are straightforward.

Equations (67) and (70) can be straightforwardly represented by $A_n^{\rm pk}$ and $B_n^{\rm pk}$, using explicit expressions for the polynomials H_{ij} and $L_n^{(\alpha)}$. The results are given by

$$b_{10} = \frac{1}{\sigma_0}\frac{\nu_{\rm c}-\gamma A_1^{\rm pk}(\nu_{\rm c})}{1-\gamma^2}, \tag{84}$$

$$b_{01} = \frac{1}{\sigma_2}\frac{-\gamma\nu_{\rm c}+A_1^{\rm pk}(\nu_{\rm c})}{1-\gamma^2}, \tag{85}$$

$$b_{20} = \frac{1}{{\sigma_0}^2}\frac{1}{1-\gamma^2}\left[\frac{\nu_{\rm c}^2-2\gamma\nu_{\rm c}A_1^{\rm pk}(\nu_{\rm c})+\gamma^2 A_2^{\rm pk}(\nu_{\rm c})}{1-\gamma^2}-1\right], \tag{86}$$

$$b_{11} = \frac{1}{\sigma_0\sigma_2}\frac{1}{1-\gamma^2} \times \left[\frac{-\gamma\nu_{\rm c}^2+(1+\gamma^2)\nu_{\rm c}A_1^{\rm pk}(\nu_{\rm c})-\gamma A_2^{\rm pk}(\nu_{\rm c})}{1-\gamma^2}+\gamma\right], \tag{87}$$

$$b_{02} = \frac{1}{{\sigma_2}^2}\frac{1}{1-\gamma^2}\left[\frac{\gamma^2\nu_{\rm c}^2-2\gamma\nu_{\rm c}A_1^{\rm pk}(\nu_{\rm c})+A_2^{\rm pk}(\nu_{\rm c})}{1-\gamma^2}-1\right], \tag{88}$$

and

$$\chi_1 = -\frac{3}{2{\sigma_1}^2}, \tag{89}$$

$$\omega_{10} = -\frac{5}{2{\sigma_2}^2}[1-B_1^{\rm pk}(\nu_{\rm c})]. \tag{90}$$

The quantities $A_1^{\rm pk}(\nu_{\rm c})$, $A_2^{\rm pk}(\nu_{\rm c})$, and $B_1^{\rm pk}(\nu_{\rm c})$ are given by one-dimensional integrals of Eqs. (78) and (79) with Eqs. (61), (81), and (83).

The above results for b_{ij} can be conveniently represented by matrix notation as follows. We note that Eq. (61) is a multivariate Gaussian function with a covariance matrix,

$$\boldsymbol{M} = \begin{pmatrix} 1 & \gamma \\ \gamma & 1 \end{pmatrix}. \tag{91}$$

Defining

$$\boldsymbol{b}^{(1)} \equiv \begin{pmatrix} \sigma_0 b_{10} \\ \sigma_2 b_{01} \end{pmatrix}, \qquad \boldsymbol{b}^{(2)} \equiv \begin{pmatrix} {\sigma_0}^2 b_{20} & \sigma_0\sigma_2 b_{11} \\ \sigma_0\sigma_2 b_{11} & {\sigma_2}^2 b_{02} \end{pmatrix}, \tag{92}$$

and

$$\boldsymbol{A}^{(1)} \equiv \begin{pmatrix} \nu_{\rm c} \\ A_1^{\rm pk}(\nu_{\rm c}) \end{pmatrix}, \qquad \boldsymbol{A}^{(2)} \equiv \begin{pmatrix} {\nu_{\rm c}}^2 & \nu_{\rm c} A_1^{\rm pk}(\nu_{\rm c}) \\ \nu_{\rm c} A_1^{\rm pk}(\nu_{\rm c}) & A_2^{\rm pk}(\nu_{\rm c}) \end{pmatrix}, \tag{93}$$

Eqs. (84)–(88) are equivalently represented by

$$\boldsymbol{b}^{(1)} = \boldsymbol{M}^{-1}\boldsymbol{A}^{(1)}, \qquad \boldsymbol{b}^{(2)} = \boldsymbol{M}^{-1}\boldsymbol{A}^{(2)}\boldsymbol{M}^{-1} - \boldsymbol{M}^{-1}. \tag{94}$$

D. Excursion set peaks

The ESP model extends the peaks model with another constraint that the smoothed linear density field should increase when the mass scale decreases, $\partial\delta_s/\partial R_s < 0$, in order to avoid the cloud-in-cloud problem. We define the normalized slope of the smoothed linear density field with respect to the smoothing radius,

$$\mu_s = -\frac{1}{\Delta_{s0}}\frac{\partial\delta_s}{\partial R_s}, \tag{95}$$

where

$$\Delta_{s0} = \left\langle \left(\frac{\partial\delta_s}{\partial R_s}\right)^2 \right\rangle^{1/2}. \tag{96}$$

The constraint of the ESP model is to require an inequality $\mu_s > 0$. The differential number density of the ESP model is given by [24,25,34]

$$n_{\rm ESP} = -\left(\frac{d\sigma_{s0}}{dR_s}\right)^{-1}\Delta_{s0}\frac{\mu_s}{\nu_s}\Theta(\mu_s)n_{\rm pk}, \tag{97}$$

where $n_{\rm pk}$ is the differential number density of discrete peaks given by Eq. (45). This implies that the multiplicity function of the excursion reads

$$f_{\rm ESP}(\nu_{\rm c}) \equiv V\nu_{\rm c}\int d^{11}y n_{\rm ESP}\mathcal{P}, \tag{98}$$

where $V = M/\bar{\rho}_0$ is the Lagrangian volume of a halo of mass M and the vector (y_α) now consists of the 11 variables $(\nu, \mu, \eta_i, \zeta_{ij})$.

Although it would be desirable to use the same window function (such as the window shape of Ref. [31] measured directly from simulations), for all the relevant fields, our approach remains perfectly consistent when different filters are applied. For instance, top-hat smoothing is not appropriate to define density peaks because the window function does not vanish sufficiently fast at high k. As a result, spectral moments like σ_2 do not converge for a cold dark matter (CDM) power spectrum. However, since top-hat smoothing is the natural choice to relate the peak height to the spherical collapse expectation, Refs. [39,40] suggested applying the top-hat window $W_{\rm T}$ the variables ν_s and μ_s and a Gaussian filter $W_{\rm G}$ to the variables η_{si} and ζ_{sij}. In the following, we denote the window function for ν_s and μ_s by $W(kR)$ and that for η_{si} and ζ_{sij} by $\bar{W}(k\bar{R})$. When a single window function is applied, one can simply set $\bar{R} = R$ and $\bar{W}(k\bar{R}) = W(kR)$. In the following, we omit the subscript s in this subsection below and use notations such as ν, μ, η_i, ζ_{ij}. The quantity σ_0 is associated with the window function of $W(kR)$, and $\bar{\sigma}_1$, $\bar{\sigma}_2$ are associated with $\bar{W}(k\bar{R})$. The rms of Eq. (96) is represented by Δ_0 with a window function of W and explicitly given by

$${\Delta_0}^2 = \int \frac{k^2 dk}{2\pi^2} k^2 [W'(kR)]^2 P_{\rm L}(k), \tag{99}$$

where $W'(x) = dW(x)/dx$ is the first derivative of the window function.

1. Derivation of renormalized bias functions in the ESP model

We define rotationally invariant quantities η^2, J_1, J_2, and J_3 as in Eq. (46). For a Gaussian initial condition, the joint probability distribution function is given by

$$\mathcal{P}(\boldsymbol{y}) \propto \mathcal{N}(\nu, J_1, \mu)\exp\left(-\frac{3}{2}\eta^2 - \frac{5}{2}J_2\right), \tag{100}$$

where $\mathcal{N}(\nu, J_1, \mu)$ is the trivariate distribution function, which is given by

$$\mathcal{N}(\nu, J_1, \mu) = \frac{1}{\sqrt{(2\pi)^3|\boldsymbol{M}|}}\exp\left(-\frac{1}{2}\boldsymbol{a}^{\rm T}\boldsymbol{M}^{-1}\boldsymbol{a}\right), \tag{101}$$

where

$$\boldsymbol{a} = \begin{pmatrix} \nu \\ J_1 \\ \mu \end{pmatrix}, \qquad \boldsymbol{M} = \begin{pmatrix} 1 & \gamma_{12} & \gamma_{13} \\ \gamma_{12} & 1 & \gamma_{23} \\ \gamma_{13} & \gamma_{23} & 1 \end{pmatrix}. \tag{102}$$

The matrix $\boldsymbol{M}$ is the covariance matrix of $\boldsymbol{a}$: $M_{ij} = \langle a_i a_j \rangle$. The variables are normalized so as to have the diagonal elements of this matrix unity. The off-diagonal elements are given by

$$\gamma_{12} = \langle \nu J_1 \rangle = \frac{1}{\sigma_0 \bar{\sigma}_2} \int \frac{k^2 dk}{2\pi^2} k^2 W(kR) \bar{W}(k\bar{R}) P_{\rm L}(k), \quad (103)$$

$$\gamma_{13} = \langle \nu \mu \rangle = -\frac{1}{\sigma_0 \Delta_0} \int \frac{k^2 dk}{2\pi^2} k W(kR) W'(kR) P_{\rm L}(k), \quad (104)$$

$$\gamma_{23} = \langle J_1 \mu \rangle = -\frac{1}{\bar{\sigma}_2 \Delta_0} \int \frac{k^2 dk}{2\pi^2} k^3 \bar{W}(k\bar{R}) W'(kR) P_{\rm L}(k). \quad (105)$$

The determinant $|\boldsymbol{M}|$ and the inverse matrix $\boldsymbol{M}^{-1}$ are given by

$$|\boldsymbol{M}| = 1 - {\gamma_{12}}^2 - {\gamma_{23}}^2 - {\gamma_{13}}^2 + 2\gamma_{12}\gamma_{23}\gamma_{13}, \quad (106)$$

$$\boldsymbol{M}^{-1} = \frac{1}{|\boldsymbol{M}|} \begin{pmatrix} 1-{\gamma_{23}}^2 & \gamma_{23}\gamma_{13}-\gamma_{12} & \gamma_{12}\gamma_{23}-\gamma_{13} \\ \gamma_{23}\gamma_{13}-\gamma_{12} & 1-{\gamma_{13}}^2 & \gamma_{13}\gamma_{12}-\gamma_{23} \\ \gamma_{12}\gamma_{23}-\gamma_{13} & \gamma_{13}\gamma_{12}-\gamma_{23} & 1-{\gamma_{12}}^2 \end{pmatrix}. \quad (107)$$

Choosing a Gaussian filter for both windows, i.e., $W(kR) = \bar{W}(k\bar{R}) = W_{\rm G}(kR)$, leads to $-kW'_{\rm G}(kR) = Rk^2 W_{\rm G}(kR)$ and $\mu = (R\bar{\sigma}_2/\Delta_0) J_1$, which signifies that μ and J_1 are redundant variables. In this special case, the third variable in $\boldsymbol{a}$ is not necessary, and we only need a two-dimensional covariance matrix. We will not consider this simpler case in what follows.

Using the fact that $\mathcal{P}$ is a function of only ν, μ, η^2, J_1, and J_2, and following the same steps of Eqs. (54)–(59), we have

$$\langle \mathcal{D}(\boldsymbol{k}) \rangle_\Omega \mathcal{P} = \left[\frac{W(kR)}{\sigma_0} \frac{\partial}{\partial \nu} + \frac{k^2 \bar{W}(k\bar{R})}{\bar{\sigma}_2} \frac{\partial}{\partial J_1} - \frac{kW'(kR)}{\Delta_0} \frac{\partial}{\partial \mu} \right] \mathcal{P}, \quad (108)$$

$$\begin{aligned} \langle \mathcal{D}(\boldsymbol{k}_1) \mathcal{D}(\boldsymbol{k}_2) \rangle_\Omega \mathcal{P} = & \left\{ \left[\frac{W(k_1R)}{\sigma_0} \frac{\partial}{\partial \nu} + \frac{k_1^2 \bar{W}(k_1\bar{R})}{\bar{\sigma}_2} \frac{\partial}{\partial J_1} - \frac{k_1 W'(k_1R)}{\Delta_0} \frac{\partial}{\partial \mu} \right] \left[\frac{W(k_2R)}{\sigma_0} \frac{\partial}{\partial \nu} + \frac{k_2^2 \bar{W}(k_2\bar{R})}{\bar{\sigma}_2} \frac{\partial}{\partial J_1} - \frac{k_2 W'(k_2R)}{\Delta_0} \frac{\partial}{\partial \mu} \right] \right. \\ & - \frac{2(\boldsymbol{k}_1 \cdot \boldsymbol{k}_2) \bar{W}(k_1\bar{R}) \bar{W}(k_2\bar{R})}{{\bar{\sigma}_1}^2} \left[1 + \frac{2}{3} \eta^2 \frac{\partial}{\partial(\eta^2)} \right] \frac{\partial}{\partial(\eta^2)} \\ & \left. + \frac{[3(\boldsymbol{k}_1 \cdot \boldsymbol{k}_2)^2 - k_1^2 k_2^2] \bar{W}(k_1\bar{R}) \bar{W}(k_2\bar{R})}{{\bar{\sigma}_2}^2} \left[1 + \frac{2}{5} J_2 \frac{\partial}{\partial(J_2)} \right] \frac{\partial}{\partial(J_2)} \right\} \mathcal{P}. \end{aligned} \quad (109)$$

Substituting Eqs. (108) and (109) into the integrand of Eq. (29), we have

$$c_X^{(1)}(k) = b_{100} W(kR) + b_{010} k^2 \bar{W}(k\bar{R}) - b_{001} kW'(kR), \quad (110)$$

$$\begin{aligned} c_X^{(2)}(\boldsymbol{k}_1, \boldsymbol{k}_2) = & \, b_{200} W(k_1R) W(k_2R) + b_{110} [k_2^2 W(k_1R) \bar{W}(k_2\bar{R}) + (1 \leftrightarrow 2)] \\ & + \{ b_{020} k_1^2 k_2^2 + \omega_{10} [3(\boldsymbol{k}_1 \cdot \boldsymbol{k}_2)^2 - k_1^2 k_2^2] - 2\chi_1 (\boldsymbol{k}_1 \cdot \boldsymbol{k}_2) \} \bar{W}(k_1\bar{R}) \bar{W}(k_2\bar{R}) \\ & - b_{101} [k_1 W'(k_1R) W(k_2R) + (1 \leftrightarrow 2)] - b_{011} [k_1 k_2^2 W'(k_1R) \bar{W}(k_2\bar{R}) + (1 \leftrightarrow 2)] + b_{002} k_1 k_2 W'(k_1R) W'(k_2R), \end{aligned} \quad (111)$$

where

$$b_{ijk} = \frac{1}{{\sigma_0}^i {\bar{\sigma}_2}^j {\Delta_0}^k \bar{n}_{\rm ESP}} \int d^{11}y n_{\rm ESP} H_{ijk}(\nu, J_1, \mu) \mathcal{P}, \quad (112)$$

$$\chi_k = \frac{(2k+1)!!}{2^k k!} \frac{(-1)^k}{{\bar{\sigma}_1}^{2k}}, \quad (113)$$

$$\omega_{l0} = \frac{(-1)^l}{{\bar{\sigma}_2}^{2l} \bar{n}_{\rm ESP}} \int d^{11}y n_{\rm ESP} L_l^{(3/2)} \left(\frac{5}{2} J_2 \right) \mathcal{P}. \quad (114)$$

Here, H_{ijk} are trivariate Hermite polynomials

$$H_{ijk}(\nu, J_1, \mu) \equiv \frac{(-1)^{i+j+k}}{\mathcal{N}(\nu, J_1, \mu)} \left(\frac{\partial}{\partial \nu} \right)^i \left(\frac{\partial}{\partial J_1} \right)^j \left(\frac{\partial}{\partial \mu} \right)^k \mathcal{N}(\nu, J_1, \mu), \quad (115)$$

and we have exploited the fact that $n_{\rm ESP}$ contains a delta function $\delta_{\rm D}^3(\boldsymbol{\eta})$ to simplify χ_i.

Again, Eqs. (110) and (111) exactly agree with the results derived independently in Refs. [18,41] in a fairly different manner.

2. Bias coefficients of the ESP model

The coefficients b_{ijk} and ω_{l0} also reduce to expressions with up to one-dimensional integrals, extending the method of Sec. III C 2. For this purpose, we define integrals,

$$A_{nm}^{\rm ESP}(\nu_{\rm c}) \equiv \frac{1}{\bar{n}_{\rm ESP}} \int d^{11}y n_{\rm ESP} {J_1}^n \mu^m \mathcal{P}, \tag{116}$$

$$B_{n}^{\rm ESP}(\nu_{\rm c}) \equiv \frac{1}{\bar{n}_{\rm ESP}} \int d^{11}y n_{\rm ESP} {J_2}^n \mathcal{P}. \tag{117}$$

Just in a similar manner of deriving Eqs. (78) and (79), Eqs. (116) and (117) reduce to

$$A_{nm}^{\rm ESP}(\nu_{\rm c}) = \frac{\int_0^\infty dx x^n f_0(x) g_m(\nu_{\rm c}, x)}{\int_0^\infty dx f_0(x) g_0(\nu_{\rm c}, x)}, \tag{118}$$

$$B_{n}^{\rm ESP}(\nu_{\rm c}) = \frac{\int_0^\infty dx f_n(x) g_0(\nu_{\rm c}, x)}{\int_0^\infty dx f_0(x) g_0(\nu_{\rm c}, x)}, \tag{119}$$

where

$$g_m(\nu_{\rm c}, x) = \int_0^\infty d\mu \mu^{m+1} \mathcal{N}(\nu_{\rm c}, x, \mu). \tag{120}$$

The function $g_m(\nu_{\rm c}, x)$ is analytically represented by the parabolic cylinder function $D_\lambda(z)$ which has an integral representation,

$$D_\lambda(z) = \frac{e^{-z^2/4}}{\Gamma(-\lambda)} \int_0^\infty e^{-zt-t^2/2} t^{-\lambda-1} dt. \tag{121}$$

For our convenience, we define a function

$$H_\lambda(z) \equiv e^{z^2/4} D_\lambda(z). \tag{122}$$

When $\lambda = n$ is a non-negative integer, this function reduces to Hermite polynomials $H_n(z)$. When $\lambda = -n$ is a negative integer, integral representation of $H_{-n}(z)$ is given by

$$\begin{aligned} H_{-n}(z) &= \frac{1}{(n-1)!} \int_0^\infty e^{-zt-t^2/2} t^{n-1} dt \\ &= \frac{\sqrt{\pi/2}}{(n-1)!} \left(-\frac{d}{dz}\right)^{n-1} \left[e^{z^2/2} \mathrm{erfc}\left(\frac{z}{\sqrt{2}}\right)\right]. \end{aligned} \tag{123}$$

First, several functions are explicitly given by

$$H_{-1}(z) = \sqrt{\frac{\pi}{2}} e^{z^2/2} \mathrm{erfc}\left(\frac{z}{\sqrt{2}}\right), \tag{124}$$

$$H_{-2}(z) = 1 - \sqrt{\frac{\pi}{2}} z e^{z^2/2} \mathrm{erfc}\left(\frac{z}{\sqrt{2}}\right), \tag{125}$$

$$H_{-3}(z) = \frac{1}{2}\left[-z + \sqrt{\frac{\pi}{2}} (z^2+1) e^{z^2/2} \mathrm{erfc}\left(\frac{z}{\sqrt{2}}\right)\right], \tag{126}$$

$$H_{-4}(z) = \frac{1}{6}\left[z^2 + 2 - \sqrt{\frac{\pi}{2}} (3z + z^3) e^{z^2/2} \mathrm{erfc}\left(\frac{z}{\sqrt{2}}\right)\right]. \tag{127}$$

Using the function $H_{-n}(z)$ defined above, an integration by μ in Eq. (120) can be analytically performed, resulting in

$$\begin{aligned} g_m(\nu_{\rm c}, x) = &\frac{(m+1)!}{\sqrt{(2\pi)^3 |\boldsymbol{M}|} (M_{33}^{-1})^{m/2+1}} \\ &\times \exp\left[-\frac{1}{2} (M_{11}^{-1} {\nu_{\rm c}}^2 + 2 M_{12}^{-1} \nu_{\rm c} x + M_{22}^{-1} x^2)\right] \\ &\times H_{-(m+2)}\left(\frac{M_{13}^{-1} \nu_{\rm c} + M_{23}^{-1} x}{\sqrt{M_{33}^{-1}}}\right), \end{aligned} \tag{128}$$

where $M_{ij}^{-1} = [\boldsymbol{M}^{-1}]_{ij}$ are matrix elements of the inverse matrix $\boldsymbol{M}^{-1}$ given by Eq. (107). Substituting Eqs. (123) and (128) into Eqs. (118) and (119), only one-dimensional numerical integrations of smooth functions are required.

Equations (112), (113), and (114) can be straightforwardly represented by functions $A_{nm}^{\rm ESP}(\nu_{\rm c})$ and $B_n^{\rm ESP}(\nu_{\rm c})$, using explicit forms of polynomials H_{ijk}, $L_i^{(\alpha)}$. As in Eqs. (91)–(94) of the peaks model, the results for b_{ijk} are conveniently represented by matrix notation. Defining

$$\boldsymbol{b}^{(1)} \equiv \begin{pmatrix} \sigma_0 b_{100} \\ \bar{\sigma}_2 b_{010} \\ \Delta_0 b_{001} \end{pmatrix}, \tag{129}$$

$$\boldsymbol{b}^{(2)} \equiv \begin{pmatrix} {\sigma_0}^2 b_{200} & \sigma_0 \bar{\sigma}_2 b_{110} & \sigma_0 \Delta_0 b_{101} \\ \sigma_0 \bar{\sigma}_2 b_{110} & {\bar{\sigma}_2}^2 b_{020} & \bar{\sigma}_2 \Delta_0 b_{011} \\ \sigma_0 \Delta_0 b_{101} & \bar{\sigma}_2 \Delta_0 b_{011} & {\Delta_0}^2 b_{002} \end{pmatrix}, \tag{130}$$

and

$$\boldsymbol{A}^{(1)} \equiv \begin{pmatrix} \nu_{\rm c} \\ A_{10}^{\rm ESP}(\nu_{\rm c}) \\ A_{01}^{\rm ESP}(\nu_{\rm c}) \end{pmatrix}, \tag{131}$$

$$\boldsymbol{A}^{(2)} \equiv \begin{pmatrix} {\nu_{\rm c}}^2 & \nu_{\rm c} A_{10}^{\rm ESP}(\nu_{\rm c}) & \nu_{\rm c} A_{01}^{\rm ESP}(\nu_{\rm c}) \\ \nu_{\rm c} A_{10}^{\rm ESP}(\nu_{\rm c}) & A_{20}^{\rm ESP}(\nu_{\rm c}) & A_{11}^{\rm ESP}(\nu_{\rm c}) \\ \nu_{\rm c} A_{01}^{\rm ESP}(\nu_{\rm c}) & A_{11}^{\rm ESP}(\nu_{\rm c}) & A_{02}^{\rm ESP}(\nu_{\rm c}) \end{pmatrix}, \tag{132}$$

we have

$$\boldsymbol{b}^{(1)} = \boldsymbol{M}^{-1} \boldsymbol{A}^{(1)}, \qquad \boldsymbol{b}^{(2)} = \boldsymbol{M}^{-1} \boldsymbol{A}^{(2)} \boldsymbol{M}^{-1} - \boldsymbol{M}^{-1}, \tag{133}$$

where $\boldsymbol{M}^{-1}$ is given by Eq. (107). All the coefficients to evaluate the renormalized bias functions up to second order in Eqs. (110) and (111) for the ESP model are thus obtained. The results for χ_1 and ω_{10} are

$$\chi_1 = -\frac{3}{2\bar{\sigma}_1{}^2}, \tag{134}$$

$$\omega_{10} = -\frac{5}{2\bar{\sigma}_2{}^2}[1 - B_1^{\rm ESP}(\nu_{\rm c})]. \tag{135}$$

IV. RESULTS

In this section, all the formulas in previous sections are put together, and the results of power spectra and correlation functions with various biasing schemes are presented. In the following, the flat ΛCDM model with cosmological parameters $\Omega_{\rm m0} = 0.3089$, $\Omega_{\rm b0} = 0.0486$, $h = 0.6774$, $n_{\rm s} = 0.9667$, $\sigma_8 = 0.8159$ (Planck2015 [42]) is assumed. We will hereafter present for the representative redshifts $z = 1$, 2, 3, which are of particular interest because currently planned, forthcoming redshift surveys will harvest this redshift range. We have checked that results at lower redshift, such as $z = 0.5$, are qualitatively similar to those at $z = 1$. Another reason for focusing at $z \geq 1$ is the fact that the applicability range of the perturbation theory decreases noticeably for $z \ll 1$.

A. Bias models

Four different models of bias are considered in this section. The "halo model" refers to a model described in Sec. III B, and the renormalized bias functions are given by Eqs. (43) and (44) with coefficients of Eq. (41). The top-hat window function $W_{\rm T}(kR)$ and the Sheth-Tormen mass function, Eq. (37), are adopted in this model. The only parameter in this model is a smoothing radius R, or equivalently a mass scale M of Eq. (33).

The "local halo" refers to a model with scale-independent values of renormalized bias functions, $c_X^{(1)} = b_1^{\rm L}$, $c_X^{(2)} = b_2^{\rm L}$, where $b_n^{\rm L}$ are given by the halo model above. This model is a simplified version of the halo model, in which the renormalized bias functions are replaced by their low-k limits. Hence, this is equivalent to completely neglecting the effects of the window function in Eqs. (43) and (44). Scale-independent bias functions correspond to a bias model in which the number density of biased tracers $n_X^{\rm L}(\boldsymbol{x})$ solely is a function of linear density field $\delta_{\rm L}(\boldsymbol{x})$ at the same Lagrangian position $\boldsymbol{x}$. We consider this model for the purpose of assessing the importance of the window functions in the halo model.

The "peaks model" refers to the model described in Sec. III C. Its renormalized bias functions are given by Eqs. (65) and (66) with coefficients calculated by Eqs. (84)–(90). A Gaussian window function $W_{\rm G}(kR_{\rm G})$ is adopted throughout. While the threshold $\nu_{\rm c}$ is originally a free parameter of the peaks model, we fix its value with a relation $\nu_{\rm c} = \delta_{\rm c}/\sigma_{\rm G0}(R_{\rm G})$, where $\sigma_{\rm G0}(R_{\rm G}) = \sigma_0(R_{\rm G})$ is the rms of variance. Therefore, the Gaussian smoothing radius $R_{\rm G}$ is the only parameter in this model.

The "ESP model" refers to a model described in Sec. III D, and the renormalized bias functions are given by Eqs. (110) and (111) with coefficients calculated by Eqs. (129)–(135). There are two kinds of window functions in this model: a top-hat and Gaussian, which we denote as $W(kR) = W_{\rm T}(kR_{\rm T})$ and $\bar{W}(k\bar{R}) = W_{\rm G}(kR_{\rm G})$, respectively. These smoothing radii are related by $R_{\rm G} = 0.46R_{\rm T}$ [40]. Furthermore, the threshold value is fixed by $\nu_{\rm c} = \delta_{\rm c}/\sigma_{\rm T0}(R)$, where $\sigma_{\rm T0}(R) = \sigma_0(R)$ is the rms of variance with the top-hat window function. Hence, the top-hat smoothing radius R is the only free parameter of this model.

Each bias model has a unique parameter in our settings described above. To make comparisons among various biasing schemes, the parameter of each model is adjusted so as to give the same value for the first-order renormalized bias function in the low-k limit, $\lim_{k\to 0} c_X^{(1)}(k)$. This limiting value is the bias parameter $b_1^{\rm L}$, b_{10}, or b_{100}, depending on the model details. For the purpose of presentation, we define the value by the parameter $b_1^{\rm L}(M)$ with the top-hat window function and a mass scale $M = 1 \times 10^{13} h^{-1} M_\odot$ in Eq. (34). The resulting values are $b_1^{\rm L} = 1.053$ ($z = 1$), 2.694 ($z = 2$), 5.039 ($z = 3$). The smoothing radii of peaks and ESP models are adjusted to reproduce the same values in b_{10} and b_{100}. The corresponding mass scale varies in the range $M = 0.7$–$1.8 \times 10^{13} h^{-1} M_\odot$ for the peaks and ESP models, with a slight dependence on redshift.

B. Renormalized bias functions

The renormalized bias functions, $c_X^{(1)}(k)$ and $c_X^{(2)}(\boldsymbol{k}_1, \boldsymbol{k}_2)$, are shown in Fig. 1. For the second-order functions, the horizontal axis corresponds to the amplitude of $|\boldsymbol{k}_1 + \boldsymbol{k}_2| \equiv k$, which is relevant to the scale of power spectrum $P(k)$. Three different shapes corresponding to the triangles $[|\boldsymbol{k}_1|, |\boldsymbol{k}_2|, |\boldsymbol{k}_1 + \boldsymbol{k}_2|] = [k, k, k], [5k, 5k, k], [k/5, k, k]$ are plotted to illustrate the characteristic behaviors. These configurations correspond to equilateral, folded, and squeezed shapes of a triangle, respectively.

The local halo model has a constant value in each panel by definition. Other models have asymptotes $c_X^{(n)} \to 0$ in large k, because the window functions vanish in this limit. This reflects the fact that the halo centers cannot have clustering power on scales smaller than the halo mass. The value of second-order parameter $b_2^{\rm L}$ turns out to be very close to zero at redshift $z = 1$ for our cosmology and fiducial mass function. Consequently, the low-k limit of the renormalized bias function in the halo model also is very close to zero.

A striking feature in the scale dependence of the renormalized bias functions is the appearance of peaks before the $c_X^{(n)}$ decay to zero in the large-k limit. The height of these peaks is generally larger at lower redshift. However, the amplitudes depend strongly on bias models. The peak height of the halo model is lower than those of

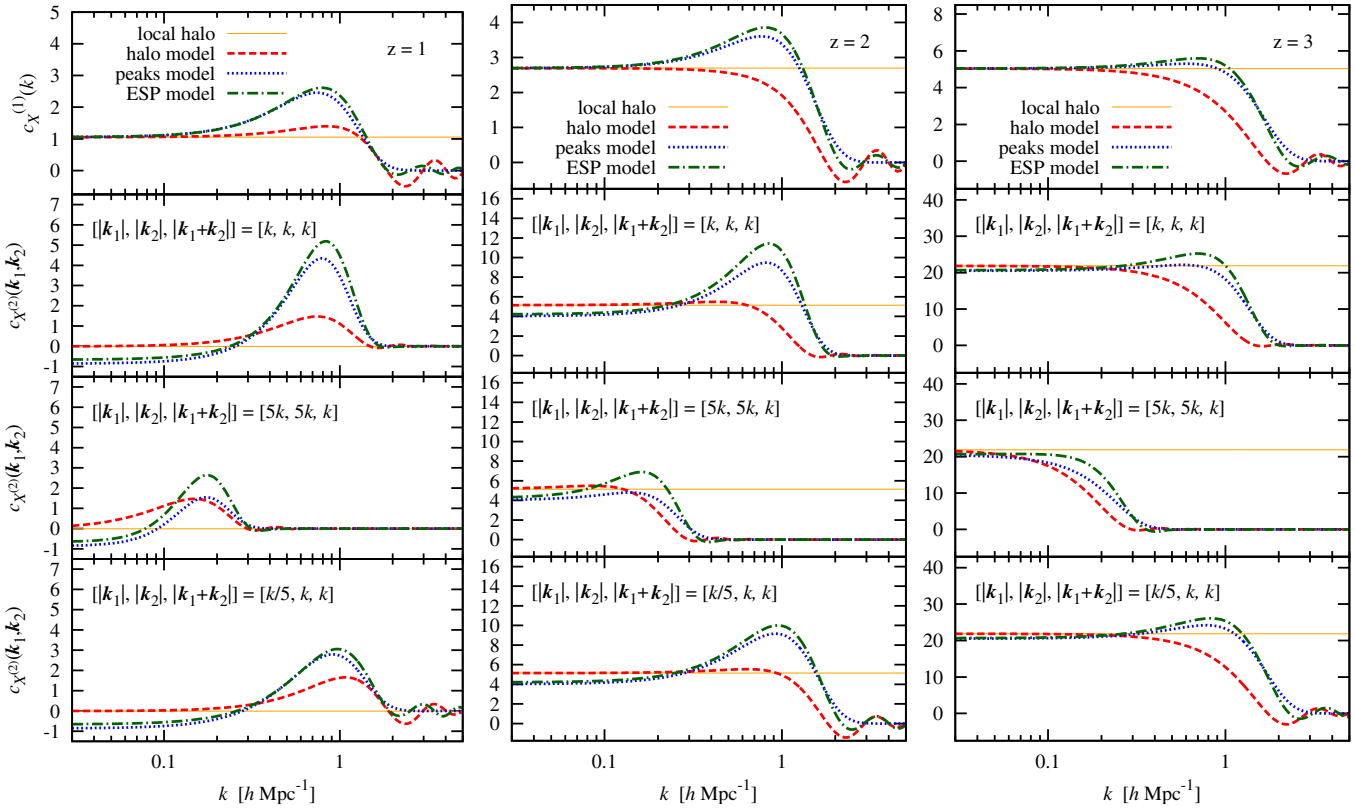

FIG. 1. Renormalized bias functions, $c_X^{(1)}$ and $c_X^{(2)}$. The results for three redshifts $z = 1, 2, 3$ are shown as indicated in each figure. Four models of bias are plotted in different lines: local halo (solid, orange), halo model (dashed, red), peaks model (dotted, blue), and ESP model (dot-dashed, green).

peaks and ESP models. There are oscillations around the asymptote in the large-k tails for halo and ESP models. These oscillations reflect the property of top-hat window function. Such oscillations are not seen in peaks model in which only Gaussian window functions are used.

The first-order renormalized bias function $c_X^{(1)}$ has recently been measured from the analysis of halos in N-body simulations [31,43]. The appearance of peaks at around $kR \sim 2.5$ and oscillating features in high-k tails are clearly observed. For instance, the behavior of the numerical results in the $z = 0.95$ sample of Ref. [31] (see its Fig. 5) lies somewhere between the predictions of the halo model and ESP model in the $z = 1$ plot of our Fig. 1: the peak height in the numerical simulations is larger than the halo model and smaller than the ESP model, and the amplitude of oscillations in the high-k tail is smaller than the halo model and larger than the ESP model. The authors of Ref. [31] use an effective window function $W_{\rm eff}$ and a model which is similar to our Eq. (43) but consider the coefficients $b_1^{\rm L}$ and $1/\delta_{\rm c}$ as free parameters. Fitting the three parameters R, $b_1^{\rm L}$, and $1/\delta_{\rm c}$ to their numerical results, the scale dependence of the Lagrangian bias factor is nicely accounted for.

One should, however, bear in mind that the precise shapes of renormalized bias functions depend on the details of the halo identification procedure. While the numerical simulations mentioned above use the "Friends-of-Friends" algorithm [44], one should naturally expect that other methods, such as the "Spherical Overdensity" algorithm [45], yield different results. Since the purpose of this paper is to investigate the impacts of different biasing schemes rather than fit our models to numerical results based on a specific halo-finding algorithm, we will keep on investigating how the four different models affect the predictions of iPT for the power spectra and correlation functions.

C. Power spectra and correlation functions in real space

Our predictions for the one-loop power spectra in real space are shown in Fig. 2. The upper panels show the power spectra divided by a no-wiggle linear power spectrum $P_{\rm nw}(k)$ [46] and by the square of Eulerian linear bias parameter, $b^2 = (1 + b_1^{\rm L})^2$. The lower panels show the scale-dependent bias, which is defined as the square root of the ratio between the power spectrum of biased tracers and that of the mass distribution, $[P_X(k)/P_{\rm m}(k)]^{1/2}$. Horizontally straight lines in bottom panels indicate the linear bias factor b. Here and henceforth, the shaded region in each figure corresponds to a rough estimate of the k range in which the one-loop iPT is inaccurate at the level of a few percent. In this figure, they are given by $k \gtrsim 0.45/\sigma_{\rm d}$,

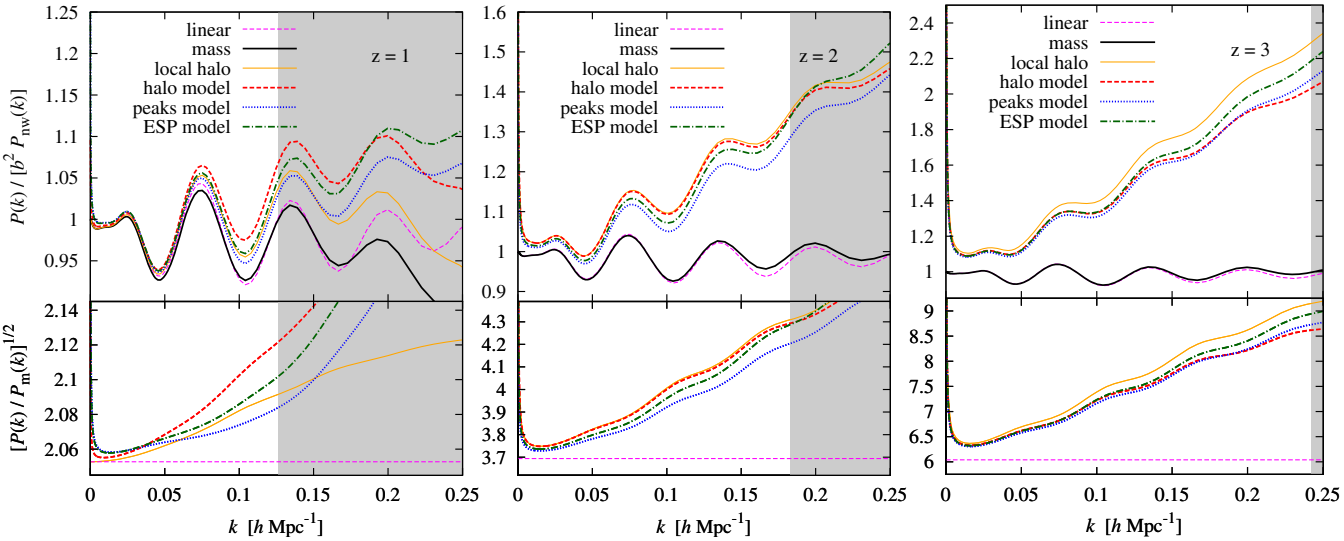

FIG. 2. The one-loop power spectra in real space with different biasing schemes. Upper panels show the power spectra divided by the linear, no-wiggle power spectrum with the linear bias, $P_X(k)/[b^2P_{\rm nw}(k)]$. The lower panels show the scale-dependent bias, $[P_X(k)/P_{\rm m}(k)]^{1/2}$. The meanings of different lines are indicated in the panels. Shaded regions represent rough estimates where the one-loop perturbation theory is expected to be inaccurate.

where $\sigma_{\rm d} = \langle|\Psi_{\rm Zel}|^2\rangle^{1/2}$ is the rms of the displacement field evaluated with the Zel'dovich approximation. Our estimate is fairly reasonable when comparison between the iPT and numerical simulations is available [47–49].

There are deviations from the predictions of linear theory even in the large-scale limit, $k < 0.01h\,{\rm Mpc}^{-1}$, owing mainly to a white-noise-like contribution generated by second-order Lagrangian bias [50]; the contribution of the first term on the rhs of Eq. (10) to the biased power spectrum of Eq. (5) is given by

$$P_X(\boldsymbol{k}) \supset \frac{1}{2}\int_{\boldsymbol{k}_{12}=\boldsymbol{k}} [c_X^{(2)}(\boldsymbol{k}_1,\boldsymbol{k}_2)]^2 P_{\rm L}(k_1)P_{\rm L}(k_2). \qquad (136)$$

The second-order bias function $c_X^{(2)}(\boldsymbol{k}_1,\boldsymbol{k}_2)$ does not generally approach zero in the large-scale limit of $\boldsymbol{k} = \boldsymbol{k}_1 + \boldsymbol{k}_2 \to \boldsymbol{0}$, and therefore the above term approaches a positive constant in the same limit. As a result, the nonlinear power spectra of biased tracers in the large-scale limit are always larger than the predictions of linear theory. At redshift $z = 1$, the second-order function is coincidentally close to zero in the large-scale limit, so that this white-noise-like term is small.

In each of our bias models, the power spectra are systematically larger than the predictions of linear theory toward small scales. Consequently, the nonlinear scale-dependent bias $[P_X(k)/P_{\rm m}(k)]^{1/2}$ increases at small scales. This property is not solely due to the scale dependencies of the first-order bias function, $c_X^{(1)}(k)$ since the local halo model, in which $c_X^{(1)}$ does not have any scale dependence, exhibits the same behavior. Therefore, the second-order effects are important to account for the scale-dependent enhancements of the power spectrum in the presence of bias.

The qualitative behavior of the power spectrum does not vary significantly among the different biasing schemes. Except for the simplistic local halo, the differences between the models are at the level of 2%–4% at $k \lesssim 0.2h\,{\rm Mpc}^{-1}$. Although the renormalized bias functions behave fairly differently among different biasing schemes, these deviations do not have a pronounced impact on the shape of the power spectrum. The reason is that the biasing schemes start deviating significantly from each other on scales smaller than the halo mass $M = 1\times10^{13}h^{-1}M_\odot$, which corresponds to $R \simeq 3h^{-1}$ Mpc or $k \sim 1h\,{\rm Mpc}^{-1}$, on which perturbation theory cannot be applied. It is the asymptotic value of the renormalized bias functions $c_X^{(n)}$ in the large-scale limit $k \to 0$ which determines the overall shape of the nonlinear power spectrum. Clearly, however, these subtle differences will be important to determine the shape of $P_X(k)$ at the percent level.

The one-loop correlation function in real space, $\xi(r)$, is plotted in Fig. 3. In the upper panels, the correlation has been multiplied by the square of the separation r^2 to highlight the shape of the baryon acoustic oscillation (BAO), as is common practice in the literature. In the lower panels, the nonlinear scale-dependent bias $[\xi_X(r)/\xi_{\rm m}(r)]^{1/2}$ is shown as a function of distance. Shaded regions correspond to the region $r \lesssim 5\sigma_{\rm d}$ where the one-loop iPT is expected to fail at a level of a few percent at least.

The upper panels indicate that the shape of the BAO peak is not significantly affected by the choice of biasing scheme. The differences on scales $r \gtrsim 20h^{-1}$ Mpc are as small as 1% at $z = 1$ and the subpercent level at $z = 2$

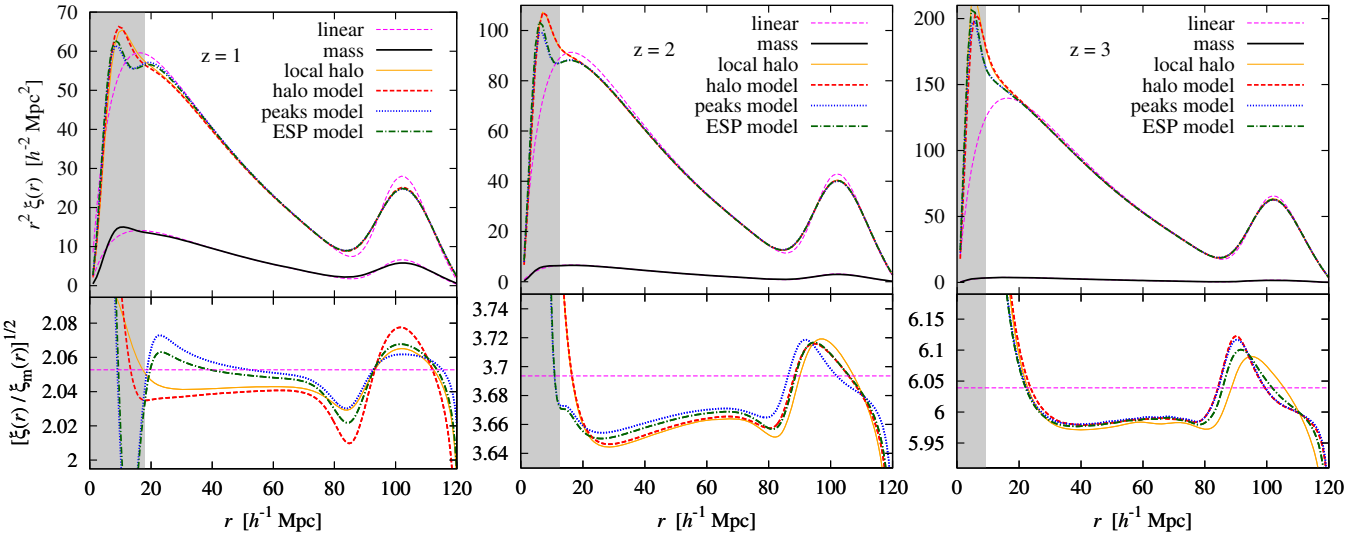

FIG. 3. The one-loop correlation functions in real space with different biasing schemes. Upper panels show the correlation functions multiplied by the square of distance, $r^2\xi_X(r)$. The lower panels show the scale-dependent bias, $[\xi_X(r)/\xi_{\rm m}(r)]^{1/2}$. Meanings of different lines are indicated in the panels. Shaded regions represent rough estimates where the one-loop perturbation theory is expected to be inaccurate.

and 3, except for the simplistic local halo. As seen in the lower panels with $z = 1$, the BAO peaks of biased tracers are slightly sharper than that of mass by a few percent. However, the shapes of the peaks for $z = 2$ and 3 are slightly distorted by a few percent in nontrivial ways. At redshift $z = 2$ and 3, the scale-dependent bias on scales 30–80h^{-1} Mpc is slightly lower than the predictions of linear theory by about 1%.

D. Power spectra and correlation functions in redshift space

The monopole components of the one-loop power spectra in redshift space are plotted in Fig. 4. In the upper panels, the results are normalized by the no-wiggle power spectrum with a linear enhancement factor b^2R_0, where $R_0 = 1 + 2\beta/3 + \beta^2/5$ is the redshift-space enhancement factor of the monopole component in linear theory [3].

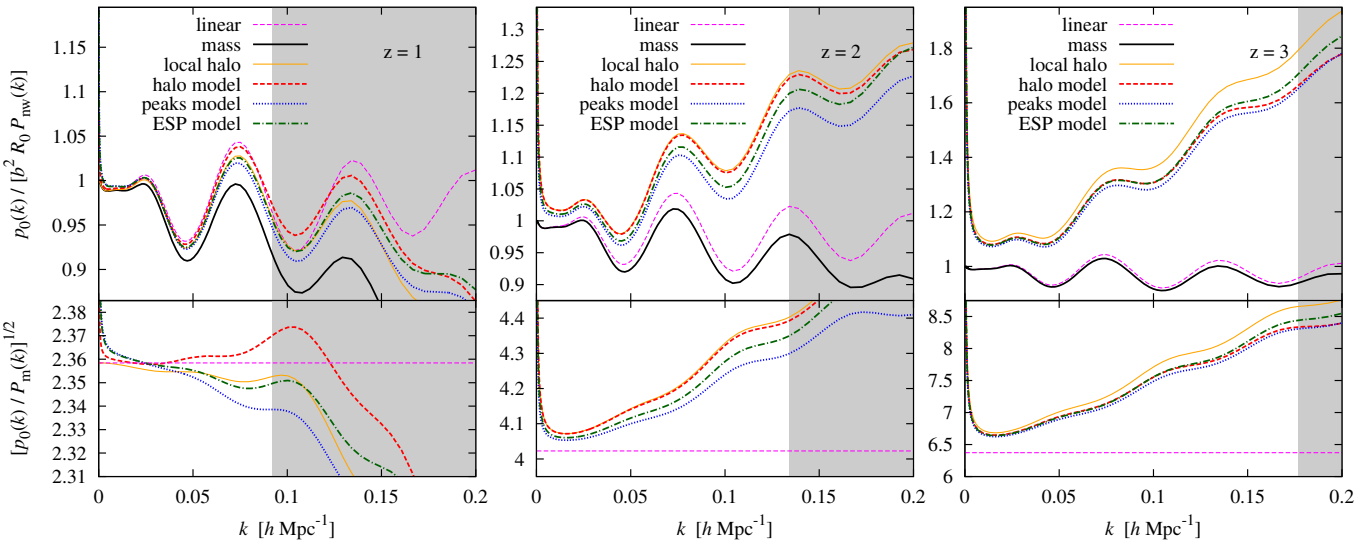

FIG. 4. The monopole components of one-loop power spectra in redshift space with different biasing schemes. Upper panels show the power spectra divided by the no-wiggle power spectrum, the linear bias parameter, and the linear redshift-space distortion factor, $p_0(k)/[b^2R_0P_{\rm nw}(k)]$. The lower panels show the scale-dependent bias in redshift space, $[p_0(k)/P_{\rm m}(k)]^{1/2}$. Meanings of different lines are indicated in the panels. Shaded regions represent rough estimates where the one-loop perturbation theory is expected to be inaccurate.

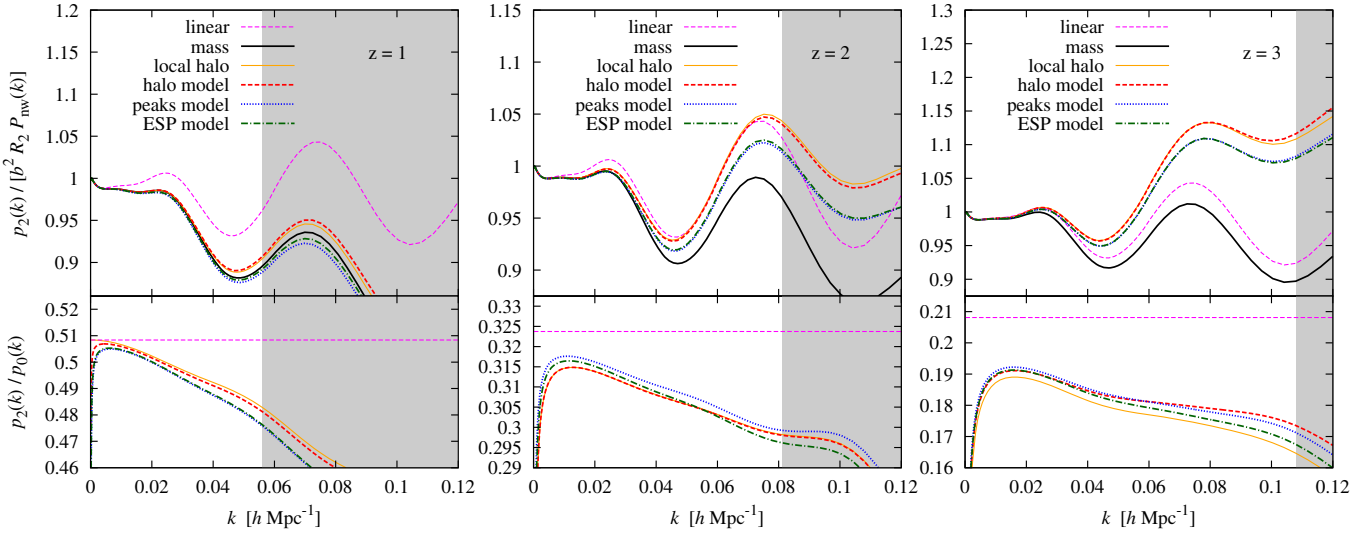

FIG. 5. The quadrupole components of one-loop power spectra in redshift space with different biasing schemes. Upper panels show the power spectra divided by the no-wiggle power spectrum, the linear bias parameter, and the linear redshift-space distortion factor, $p_0(k)/[b^2 R_2 P_{\rm nw}(k)]$. The lower panels show the ratio between the quadrupole components and the monopole components.

Again, the shaded regions correspond to $k \gtrsim 0.33/\sigma_{\rm d}$, for which the one-loop iPT is not expected to apply at the level of a few percent.

Comparing the behaviors of monopole components in redshift space with those of Fig. 2 in real space shows that the nonlinear enhancements at smaller scales are less pronounced in redshift space. Overall, however, the impact of nonlinearities is similar to that in real space. The differences among different biasing schemes are about 2%–4% at $k \lesssim 0.2h\,{\rm Mpc}^{-1}$ except for the simplistic local halo, i.e., at the same level as in real space.

The quadrupole and hexadecapole components of the one-loop power spectra in redshift space are shown in Figs. 5 and 6. In the upper panels, the additional normalization factor induced by the linear redshift-space distortions are $R_2 = 4\beta/3 + 4\beta^2/7$ and $R_4 = 8\beta^2/35$. In the lower panels, ratios of the quadrupole and hexadecapole to the monopole component are shown. These ratios are commonly used for constraining the nature of gravity through a measurement of the redshift-space distortion parameter β (e.g., Refs. [51,52]). Estimates of the applicability of iPT for the quadrupole and hexadecapole components are relatively uncertain, because a detailed comparison between the iPT and numerical simulations is not available in the literature. Therefore, we have tentatively defined the confidence region as $k < 0.2/\sigma_{\rm d}$ for the quadrupole and $k < 0.18/\sigma_{\rm d}$ for the hexadecapole. Although the multipole components appear to behave strangely at smaller scales, we warn the reader that our criteria may be inaccurate.

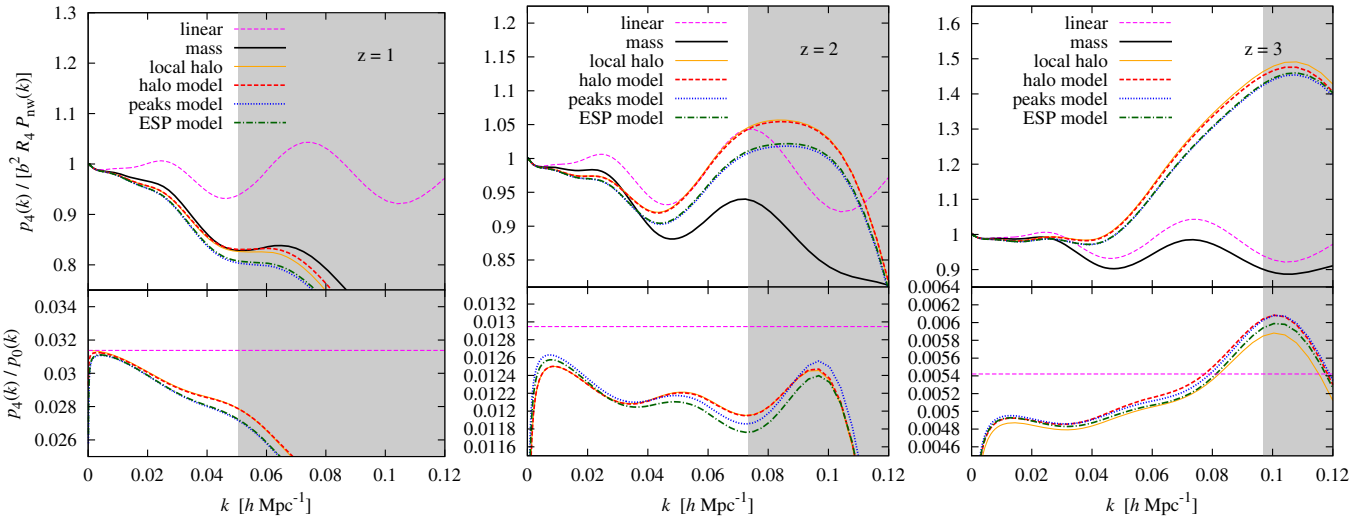

FIG. 6. Same as Fig. 5, but for the hexadecapole components.

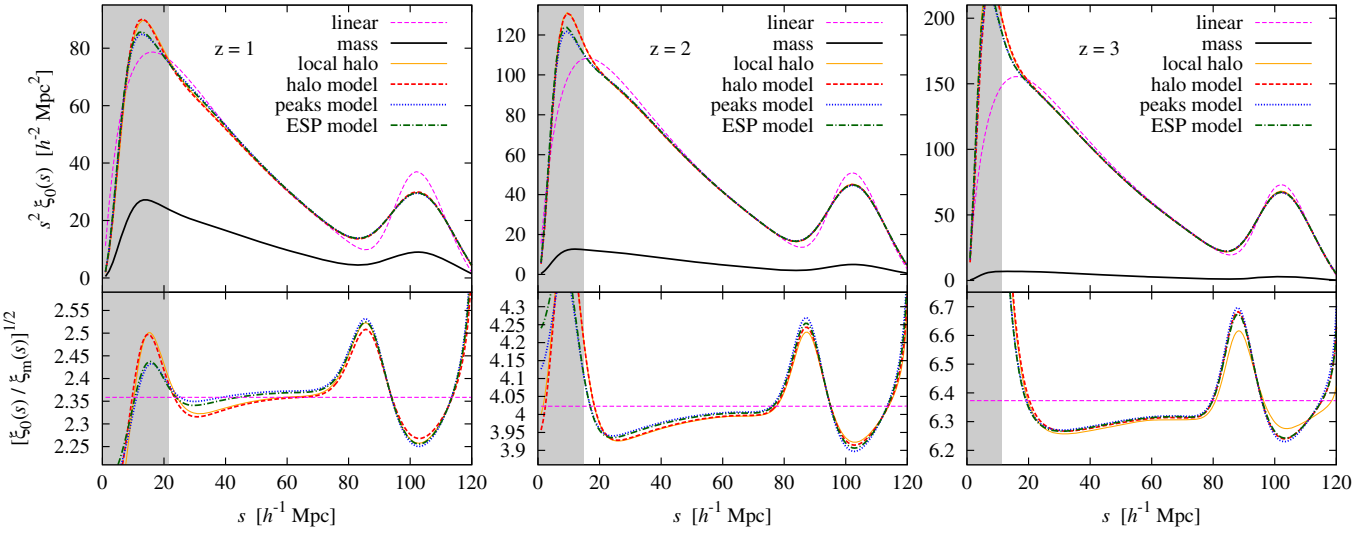

FIG. 7. The monopole components of one-loop correlation function in redshift space with different biasing schemes. Upper panels show the monopole functions multiplied by the square of distance, $s^2\xi_0(s)$. The lower panels show the scale-dependent bias in redshift space, $[\xi_0(s)/\xi_m(s)]^{1/2}$.

The variances among different biasing schemes are at most at the level of a few percent, as is the case of the monopole component. The multipole-to-monopole ratios show relatively large deviations from the predictions of linear theory, R_l/R_0. The nonlinear ratios are smaller than the linear predictions by 5%–15% even on a scale as large as $k \simeq 0.06h\,\mathrm{Mpc}^{-1}$ usually considered to belong to the linear regime. When the bias factor is large, which is the case at redshift $z = 2$ and 3, the ratios never attain the linear values at any scale. Since the ratios of linear theory, R_2/R_0 and R_4/R_0, are increasing functions of β, a blind application of linear theory to the power spectrum in redshift space would result in an underestimation of the β parameter if the bias factor were fixed (in actual analyses, however, the bias parameter is simultaneously fitted to the data). Notwithstanding, the deviations from the linear ratios are much larger than the variances among biasing schemes. The iPT provides a way to quantify the systematic effects produced by the weakly nonlinear evolution fairly independently of the biasing schemes.

In Figs. 7–9, the monopole, quadrupole, and hexadecapole of the halo correlation functions in redshift space are plotted. Our estimates for the applicability of our one-loop iPT prediction are $r < 6\sigma_d$, $r < 12\sigma_d$, and $r < 15\sigma_d$ for the

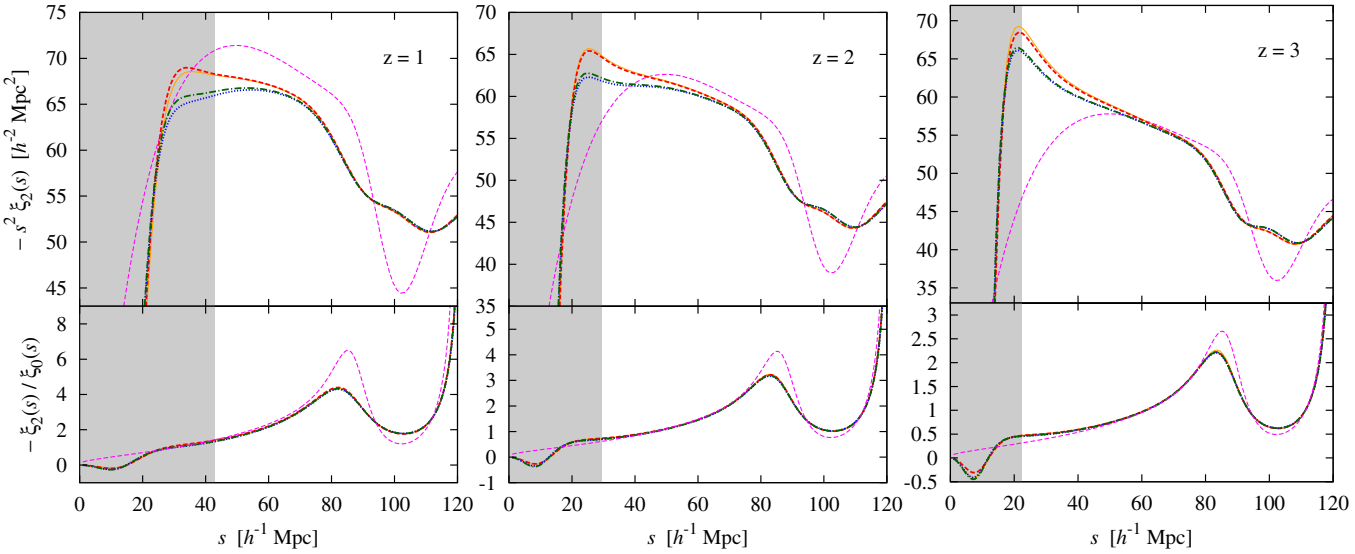

FIG. 8. The quadrupole components of one-loop correlation functions in redshift space with different biasing schemes. Upper panels show the quadrupole functions multiplied by the minus square of distance, $-s^2\xi_2(r)$. The lower panels show the ratio between the quadrupole components and the monopole components.

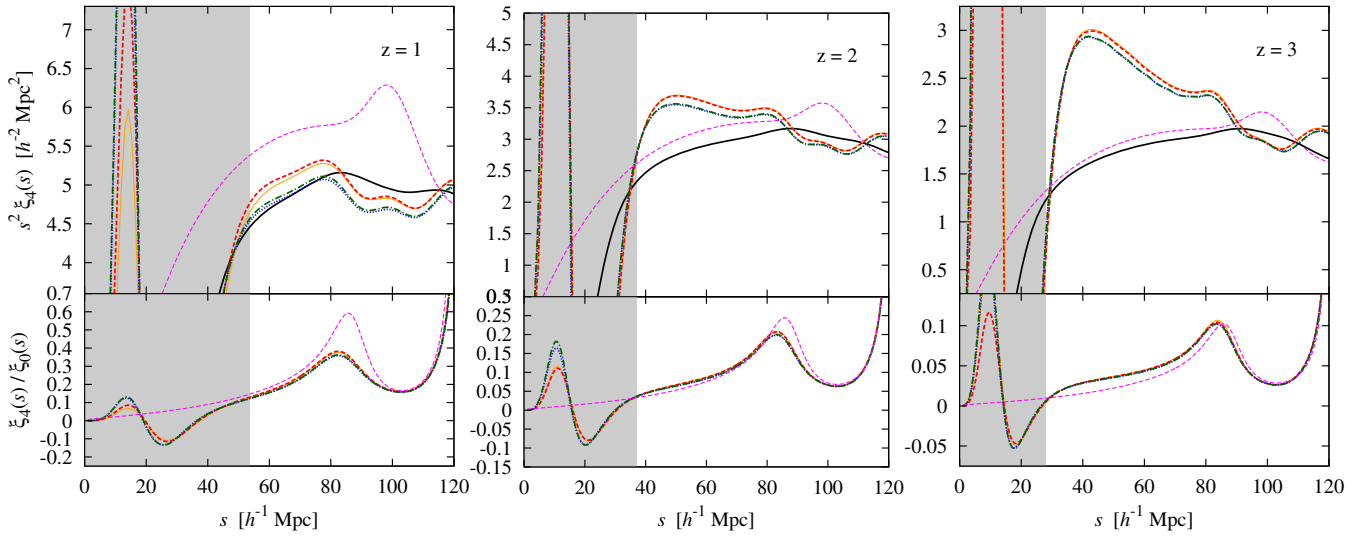

FIG. 9. Same as Fig. 8, but for the hexadecapole components.

monopole, quadrupole, and hexadecapole components, respectively. While these bounds are estimated by extrapolating the comparisons of Ref. [47], they could be inaccurate, especially in the case of hexadecapole.

The variances of different biasing schemes are within a few percent as in the case of the previous figures. The BAO peaks of the monopole components in redshift space are smoother than those in real space. Accordingly, the scale-dependent bias $[\xi_0(r)/\xi_{\rm m}(r)]^{1/2}$ varies more than those in real space. This effect of BAO smoothing does not significantly depend on the biasing schemes (except for the simplistic local halo, as usual).

Differences between the quadrupole and hexadecapole predicted by the halo and peaks/ESP models can be seen in the upper panels of Figs. 8 and 9. However, they have a similar degree of deviations as that seen in the monopole components in Fig. 7, where it is less apparent because the scales of vertical axes are much larger. The lower panels show that deviations in the quadrupole-to-monopole and hexadecapole-to-monopole ratios among the different biasing schemes are extremely small in the correlation functions in redshift space.

E. Scale-dependent bias in the presence of non-Gaussianity

If some amount of inflationary non-Gaussianity is imprinted in the initial cosmological perturbations, then the bispectrum of the linear density field receives a non-trivial primordial contribution, $B_{\rm L}(k_1,k_2,k_3)$. When this primordial bispectrum is strongly scale dependent, as in, for instance, the case for local-type non-Gaussianity, Fourier modes of the density fluctuations with long and short wavelengths, i.e., with wave numbers $k_l \ll k_s$, are coupled to each other. As a result, the power spectrum of biased tracers is affected on very large scales as it depends on the biasing processes which are small-scale phenomena [8,53,54]. In the iPT formalism, the contributions are given by the last term in Eq. (5), the general implications of which are discussed in Ref. [30].

The primordial non-Gaussianity also changes the precise shapes of the renormalized bias functions through the multivariate distribution function $\mathcal{P}(\boldsymbol{y})$; see Eqs. (29) and (30). However, this effect is small enough because the shapes of the renormalized bias functions are dominantly determined by Gaussian components [30]. For instance, the non-Gaussian corrections to $c_X^{(2)}$ are at the level of $10^{-5}f_{\rm NL}$. By contrast, the scale-dependent bias on very large scales predominantly arises from the primordial non-Gaussianity. Hence, we will neglect the subdominant corrections to the renormalized bias functions due to primordial non-Gaussianity for simplicity.

In Fig. 10, one-loop power spectra and correlation functions are shown for the different biasing schemes. We focus on the monopole component in redshift space, as it is a quantity observed in actual redshift surveys. The primordial non-Gaussianity is assumed to be of local, quadratic type, so that the primordial bispectrum takes the form

$$B_{\rm L}(k_1,k_2,k_3)=2f_{\rm NL}\left[\frac{\mathcal{M}(k_3)}{\mathcal{M}(k_1)\mathcal{M}(k_2)}P_{\rm L}(k_1)P_{\rm L}(k_2)+{\rm cyc.}\right], \tag{137}$$

where

$$\mathcal{M}(k)=\frac{2}{3}D_+(z)\frac{k^2T(k)}{{H_0}^2\Omega_{\rm m0}} \tag{138}$$

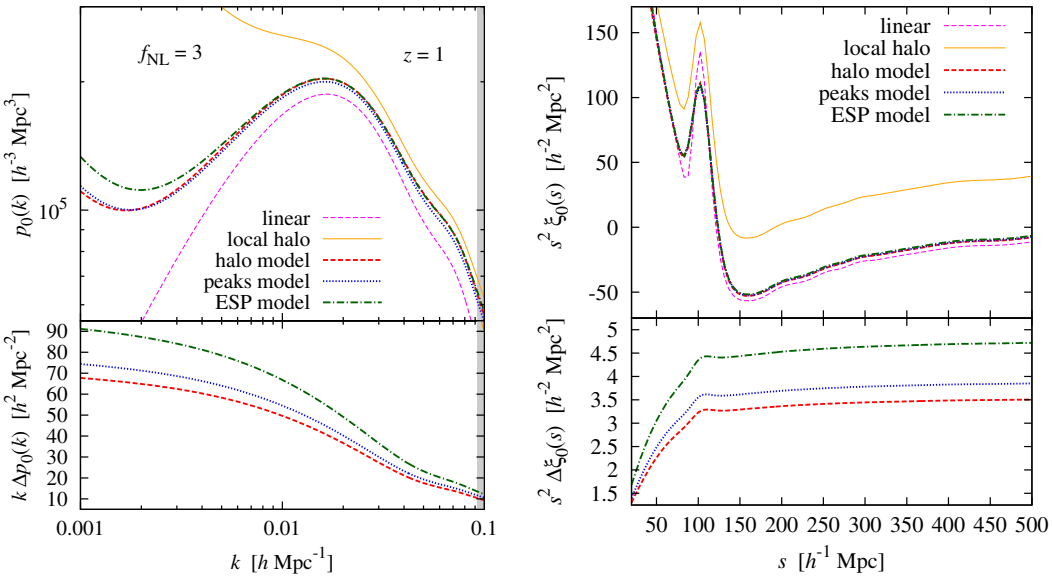

FIG. 10. Effects of primordial non-Gaussianity on the power spectra (left) and correlation functions (right) of monopole components in redshift space at the redshift of $z = 1$. Local-type non-Gaussianity with $f_{\rm NL} = 3$ is assumed. Upper panels show the monopole components of power spectra and correlation functions. Lower panels show the pure contributions from the primordial non-Gaussianity.

is the transfer function between the potential deeply in matter domination and the linear density. Here, D_+ is a linear growth factor, normalized as $D_+ \to a$ in the matter-dominated epoch, and $T(k)$ is the linear transfer function, normalized to $T(k) \to 1$ in the limit $k \to 0$. The parameter $f_{\rm NL}$ is observationally constrained to be $f_{\rm NL} = 0.8 \pm 5.0$ (68% C.L.) [55]. For illustration purposes, we assume $f_{\rm NL} = 3$ consistent with the observational bound.

In the large-scale limit, $k \to 0$, the contribution of local-type primordial non-Gaussianity to the monopole power spectrum is given by [30]

$$\Delta p_X^0(k) \approx 4 f_{\rm NL}\left(1 + c_X^{(1)}(k) + \frac{f}{3}\right)\frac{P_{\rm L}(k)}{\mathcal{M}(k)} \times \int \frac{d^3p}{(2\pi)^3}\, c_X^{(2)}(\boldsymbol{p}, -\boldsymbol{p}) P_{\rm L}(p), \tag{139}$$

where $\Delta p_X^0(k) = p_X^0(k) - p_X^{0\rm G}(k)$ and $p_X^{0\rm G}(k)$ is the Gaussian contribution with $f_{\rm NL} = 0$. The simplistic local halo [$c_X^{(2)}(\boldsymbol{p}, -\boldsymbol{p}) = \text{const}$] gives a logarithmically divergent result for the above equation if $n_{\rm s} = 1$ because $P_{\rm L}(k) \propto k^{n_{\rm s}-4}$ in the limit of $k \to \infty$ for ΛCDM models. Since the spectral index $n_{\rm s} = 0.9667$ is slightly less than unity, the above integral in the simplistic local halo converges, although it is much larger than other schemes in which the renormalized bias functions are suppressed by window functions in the small-scale limit. Thus, the effects of primordial non-Gaussianity on very large scales depend not only on the asymptotic values of $c_X^{(n)}$ but also on their shape at small scales. However, while the amplitude of Δp_X^0 strongly depends on the biasing schemes, the power-law scaling of the scale dependence in the large-scale limit, $\Delta p_X^0 \propto P_{\rm L}(k)/\mathcal{M}(k) \propto k^{n_{\rm s}-2}$, does not depend on biasing schemes. Note that the constant term Eq. (136) also contributes to the power spectra in the large-scale limit, $k \to 0$, in addition to the non-Gaussian contribution with which it is partly degenerate.

The non-Gaussian bias amplitude Eq. (139) is consistent with the peak-background expectation $\partial \ln n/\partial \ln \sigma_8$ obtained by Ref. [54] for the peaks and ESP implementations considered here (Ref. [34]; see, however, the discussion of Ref. [56] for moving stochastic barriers). However, substituting Eq. (40) into Eq. (139) shows that this is generally not the case of the local and halo models, unless the multiplicity is of the Press-Schechter form.

In the lower panel of the left figure, contributions from the primordial non-Gaussianity $\Delta p_X^0(k)$ are shown. Variations among the biasing schemes can be seen. They are not significant, except for the local halo. Still, if a nonlinear parameter $f_{\rm NL} \neq 0$ were detected, the different biasing schemes would change its estimated value by ∼25%.

In the right figure, the monopole components of the correlation function in redshift space are shown. The primordial non-Gaussianity slightly increases the correlation functions on large scales $s \gtrsim 100h^{-1}$ Mpc in a scale-dependent way, approximately $\Delta\xi_X^0(s) \propto s^{-2}$. The simplistic local halo even boosts the amplitude on the BAO scales by about 100%, which is much larger than what is measured in N-body simulations (see, e.g., Ref. [57]). The variance among other biasing schemes in $\Delta\xi_X^0$ is about 25%, in accordance with the result of Δp_X^0.

V. CONCLUSIONS

Using the iPT formalism, we have studied the impact of biasing schemes on the power spectra and correlation functions of biased tracers in the weakly nonlinear regime. In this paper, we have focused on three representative bias schemes: the halo, peaks, and ESP models. We have also considered a simplified version of the halo model in which the renormalized bias functions are assumed to be scale independent. This has allowed us to quantify the impact of the scale dependence of the bias functions on the power spectra and correlation functions.

In the iPT, all the degrees of freedom of different biasing schemes are contained in a series of renormalized bias functions. The biasing schemes we considered in this paper are semilocal models, in which the number density of biased tracers at a Lagrangian position is determined by the smoothed linear density field and its spatial derivatives at the same Lagrangian position. After deriving a compact formula to evaluate the renormalized bias functions in semilocal models of bias, these functions in individual biasing schemes are derived up to second order. Our results agree with previous works and show that the coefficients of the perturbative peaks and ESP bias expansions are associated with the iPT renormalized bias functions. In order to efficiently evaluate the renormalized bias functions, we have provided analytic reductions of various integrals in coefficients of the bias functions, so that all the coefficients are given by one-dimensional integrals with sufficiently smooth functions of integrands.

We have compared the renormalized bias functions of different biasing schemes. The $c_X^{(n)}$ of all the models (except for the simplistic local halo, which is not physically motivated) converge toward zero in the high-k limit because of the window functions. While the low-k limit of the first-order function, $c_X^{(1)}$, is the same for all models by construction, differences among biasing schemes can be seen in the low-k limit of the second-order functions $c_X^{(2)}$. These differences are, however, not very significant.

By contrast, the behaviors of the renormalized bias functions around and below the smoothing scales, $kR \gtrsim 1$, vary noticeably among the bias models. Notwithstanding, they all exhibit a peak around $kR \sim 2.5$ in lower redshifts. The presence of oscillations in the Lagrangian bias functions of low redshift halos can actually be seen in the outcome of N-body simulations [31,43]. The amplitude of the peaks in functions $c_X^{(n)}$ strongly depends on the biasing schemes or how biased tracers are identified in simulations/observations.

However, we have found that the various schemes, including the unphysical local halo, do not change the qualitative behavior of the one-loop power spectra and correlation functions. While, in the power spectra, differences are at the level of 2%–4%, they are as small as 1% on scales $r \gtrsim 20h^{-1}$ Mpc in the $z = 1$ correlation function and subpercent at higher redshift. This partly follows from the fact that the shape of the power spectra is more affected by nonlinearities than correlation functions. Furthermore, the simplistic local halo performs comparably well, confirming that the scale dependence of the renormalized bias functions is not the decisive factor governing the shape of the power spectra and correlation functions.

These conclusions also hold in redshift space, with the caveat that the distortions induced by peculiar velocities are accounted for by the Kaiser formula. The quadrupole and hexadecapole components exhibit almost the same level of differences among biasing schemes as the monopole components. The multipoles-to-monopole ratios in the power spectra, which are scale independent in linear theory, become scale dependent due to nonlinear effects. In addition, the ratios are significantly smaller than the prediction of linear theory by 5%–15% even at $k \simeq 0.06h\,\mathrm{Mpc}^{-1}$. This illustrates the importance of including nonlinear effects when estimating the redshift-space distortion parameter β. Of course, a realistic calculation should include the virial motions of galaxies within halos.

We have also estimated the effects of local-type non-Gaussianity in the initial conditions for the various biasing schemes. In this case, the simplistic local halo biasing scheme, in which small-scale filtering is absent, is inappropriate. The primordial non-Gaussianity adds power through the mode coupling between large and small scales, such that the behavior of renormalized bias functions at small scales can critically affect the power spectrum on very large scales. The amplitude of the non-Gaussian bias does not differ significantly among the other bias schemes, with deviations no larger than 25% both in the power spectra and correlation functions.

Before concluding, let us emphasize that, for the peaks and ESP models, the linear velocities are biased owing to the coupling between the velocity $\partial^{-1}\delta$ and $\partial\delta$ [26]. This statistical bias affects the redshift space distortions [58] as well as the two-point correlation around the BAO scales [27]. While it is difficult to measure this effect in numerical simulations (see, e.g., the discussion in Ref. [59]), several lines of evidence indicate that it is present in the Lagrangian space [43,60] and remains constant throughout time [43]. Although we did not highlight it explicitly, this effect is already included in the iPT. We plan to address this important issue in more details in future work.

ACKNOWLEDGMENTS

T. M. acknowledges support from MEXT KAKENHI Grants No. 15K05074 (2015) and No. 15H05890 (2015). V. D. acknowledges support from the Swiss National Science Foundation.

APPENDIX A: THE AUXILIARY FUNCTION $\Xi(\delta_M - \delta_c, \sigma_M)$ IN THE SIMPLE HALO MODEL

In the simple halo model of Sec. III B, we have introduced an auxiliary function $\Xi(\delta_M - \delta_c, \sigma_M)$. This function is a phenomenological alternative to the step function Θ designed to produce a mass function more general than the PS one. The mass function may not be universal. As explained in the main text, we do not need its actual form in deriving the renormalized bias functions. However, one may wonder whether this auxiliary function exists for an arbitrary mass function. In this Appendix, we discuss some details of the relation between the auxiliary function and the mass function.

The differential mass function $n(M)$ is given by Eq. (36). This defines the multiplicity function $f(\nu)$, which we assume universal in what follows,

$$n(M) = \frac{\bar{\rho}_0}{M}\frac{f(\nu)}{\nu}\frac{d\nu}{dM}, \tag{A1}$$

where $\nu = \delta_c/\sigma$, and we denote $\sigma = \sigma_M$ for simplicity. In our simple halo model, the localized differential number density of halos at a Lagrangian position $\boldsymbol{x}$ is given by Eq. (39), i.e.,

$$n(\boldsymbol{x}, M) = -\frac{2\bar{\rho}_0}{M}\frac{\partial}{\partial M}\Xi[\delta(\boldsymbol{x}) - \delta_c, \sigma], \tag{A2}$$

where we denote $\delta(\boldsymbol{x}) = \delta_M(\boldsymbol{x})$ for simplicity. Both δ and σ depend on the mass M through the smoothing kernel, and the partial derivative $\partial/\partial M$ applies with fixed δ_c. The PS mass function corresponds to the case that the function $\Xi(\delta - \delta_c, \sigma)$ is given by a step function $\Theta(\delta - \delta_c)$. Substituting the step function by the general function Ξ corresponds to adopting a fuzzy barrier for the identification of the collapsed regions. Therefore, it is desirable to have the same asymptotes as the step function,

$$\Xi(x, \sigma) \to \begin{cases} 0 & (x \to -\infty) \\ 1 & (x \to +\infty) \end{cases}, \tag{A3}$$

while the transition between the two limits can be arbitrary.

The above model of a fuzzy barrier is closely related to the model of square-root stochastic moving barrier [40,61,62], where the barrier is replaced by $B = \delta_c + \beta\sigma$ and β is a stochastic variable with a probability distribution function $p(\beta)$. With this model, the sharp barrier represented by the step function $\Theta(\delta - \delta_c)$ in the PS formalism is replaced by

$$\Theta(\delta - \delta_c) \to \int d\beta\, p(\beta)\Theta(\delta - \delta_c - \beta\sigma) = \Phi\left(\frac{\delta - \delta_c}{\sigma}\right), \tag{A4}$$

where $\Phi(\beta) = \int_{-\infty}^{\beta} p(\beta')d\beta'$ is the cumulative distribution function of β. Thus, the square-root stochastic moving barrier corresponds to choosing the function $\Xi(x, y) = \Phi(x/y)$.

The mass fraction of the halos with a mass greater than M is given by

$$\frac{1}{\bar{\rho}_0}\int_M^\infty n(M)M dM = \int_\nu^\infty \frac{f(\nu)}{\nu}d\nu \equiv F(\nu), \tag{A5}$$

which corresponds to the filling factor of collapsed regions in Lagrangian space. Because the ensemble average of Eq. (A2) should give the global mass function, $n(M) = \langle n(M, \boldsymbol{x})\rangle$, the auxiliary function should satisfy

$$\langle \Xi(\delta - \nu\sigma, \sigma)\rangle = \frac{1}{2}F(\nu) \tag{A6}$$

or

$$F(\nu) = 2\int_{-\infty}^{\infty} \Xi(\delta - \nu\sigma, \sigma)P_\sigma(\delta)d\delta, \tag{A7}$$

where $P_\sigma(\delta)$ is the one-point probability distribution function of δ. This distribution function explicitly depends on the mass M through σ. Applying a partial differentiation $\partial/\partial\delta_c|_\sigma = \sigma^{-1}\partial/\partial\nu|_\sigma$ to Eq. (A7) with σ fixed, and performing integration by parts, we arrive at the relation

$$\frac{f(\nu)}{\nu} = -2\sigma\int_{-\infty}^{\infty} \Xi(\delta - \nu\sigma, \sigma)\frac{\partial P_\sigma(\delta)}{\partial\delta}d\delta. \tag{A8}$$

The rhs of Eq. (A7) is a convolution integral of the function $\Xi(x, \sigma)$ and $P_\sigma(x)$ for a fixed value of σ. Thus, obtaining the auxiliary function Ξ from the mass function requires the deconvolution, the inverse problem of the convolution integral. Deconvolution is an ill-posed problem, because the solution is not unique in general: sometimes the solution does not exist, and sometimes there are many solutions. Therefore, it is not guaranteed that the solution of Eq. (A7) can be found for arbitrary function $F(\nu)$ [equivalently, for arbitrary function $f(\nu)$].

Nevertheless, numerically fitted mass functions, such as the Sheth-Tormen (ST) mass function, are derived from a finite range of ν, i.e., $0.7 \lesssim \nu \lesssim 3.5$ [36]. Thus, trying to invert the convolution integral, Eq. (A7), from the mass function extrapolated to all ranges of $0 < \nu < \infty$ is not what we should do. Instead, it is sufficient to find a reasonable kernel function Ξ which can reproduce the mass function in finite ranges of interest where a fitting formula applies. Numerically, the deconvolution techniques are widely used in signal/image restorations, e.g., a simple iterative method known as the Richardson-Lucy deconvolution [63,64].

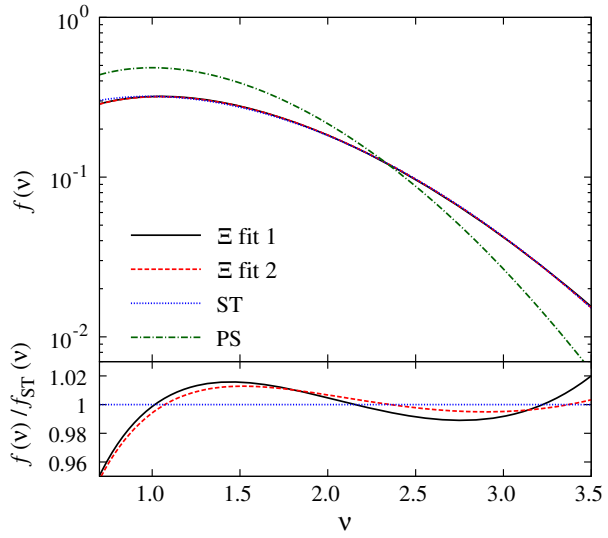

FIG. 11. The multiplicity functions derived by the model of the auxiliary function, $\hat{\Xi}(x) = 1/(e^{-1.802x} + 1)^{1.882}$ (Ξ fit 1, solid line) and $\hat{\Xi}(x) = \mathrm{erfc}[-(x - 0.4778)/(0.7671\sqrt{2})]$ (Ξ fit 2, dashed line), which are fitted to give the Sheth-Tormen mass function (dotted line). The case of Press-Schechter mass function (dot-dashed line) is also shown as a reference.

For Gaussian initial conditions, the distribution function is given by $P_\sigma(\delta) = (2\pi\sigma^2)^{-1/2} e^{-\delta^2/2\sigma^2}$. Changing the integration variable as $\delta \to t = \delta/\sigma$ in this case, the rhs of Eq. (A7) reduces to $(2/\pi)^{1/2} \int \Xi(t\sigma - \nu\sigma, \sigma) e^{-t^2/2} dt$. Since the lhs is a function of only ν, the function $\Xi(t\sigma - \nu\sigma, \sigma)$ in the integrand should not depend on σ. This condition is represented by $\partial\Xi(t\sigma, \sigma)/\partial\sigma = 0$ with t fixed, which is equivalent to a partial differential equation $x\partial\Xi(x, y)/\partial x + y\partial\Xi(x, y)/\partial y = 0$. Its general solution is given by $\Xi(x, y) = \hat{\Xi}(x/y)$, where $\hat{\Xi}$ is an arbitrary, single-valued function. Therefore, we have

$$\Xi(\delta - \delta_c, \sigma) = \hat{\Xi}\left(\frac{\delta - \delta_c}{\sigma}\right), \tag{A9}$$

in order to have a universal mass function in Gaussian initial conditions. If we use the form of Eq. (A9) in non-Gaussian initial conditions, the mass function does not have the universal form, and the resulting multiplicity function has an additional dependence of σ, which arises from the additional dependence of mass in $P_\sigma(\delta)$ through higher-order cumulants. The model of Eq. (A4) is consistent with the form of Eq. (A9), and the function $\hat{\Xi}$ is identified as the cumulative distribution function of the stochastic moving barrier, $\Phi(\beta)$. If the function $\Xi(\delta - \delta_c, \sigma)$ were to not explicitly depend on σ and $\Xi(x, y) = \Xi(x)$ were independent of y, the above differential equation would become $x\partial\Xi(x)/\partial x = 0$. The unique solution with a condition like Eq. (A3) is the step function $\Xi(x) = \Theta(x)$, which corresponds to the PS mass function. Thus, the explicit dependence of the mass in the auxiliary function Ξ is necessary to obtain non-PS mass functions. Adopting Eq. (A9) in Gaussian initial conditions, Eq. (A7) and (A8) reduce to

$$F(\nu) = \sqrt{\frac{2}{\pi}} \int_{-\infty}^{\infty} \hat{\Xi}(x - \nu) e^{-x^2/2} dx, \tag{A10}$$

$$\frac{f(\nu)}{\nu} = \sqrt{\frac{2}{\pi}} \int_{-\infty}^{\infty} \hat{\Xi}(x - \nu) x e^{-x^2/2} dx. \tag{A11}$$

Rather than deconvolving Eq. (A8) in some way, it is more straightforward to find a fitting formula of Ξ which can reproduce the required mass function. As a demonstration, let us try to find an approximate solution by assuming a simple functional form,

$$\hat{\Xi}(x) = \frac{1}{(e^{-ax} + 1)^b}, \tag{A12}$$

where $a > 0$ and $b > 0$ are fitting parameters and Gaussian initial conditions are assumed. This function has the desirable asymptotes of Eq. (A3). For a given mass function with a finite range of ν, one can fit the parameters to approximately reproduce Eq. (A11). We find the best fit parameters to reproduce the ST mass function in the range $0.7 \le \nu \le 3.5$, which corresponds to the fitted range of the fitting formula [36], to be $a = 1.802$ and $b = 1.882$. The resulting mass function is shown in Fig. 11 (Ξ fit 1). It is seen that the ST mass function is precisely recovered within a few percent.

For another trial function, we consider

$$\hat{\Xi}(x) = \frac{1}{2} \mathrm{erfc}\left[-\frac{x - \mu}{\sqrt{2}s}\right], \tag{A13}$$

where μ and $s > 0$ are fitting parameters. This function is a cumulative Gaussian distribution function with a mean μ and a variance s^2 and also satisfies the property of Eq. (A3). The best fit parameters in this case are given by $\mu = 0.4778$ and $s = 0.7671$. The resulting mass function is also shown in Fig. 11 (Ξ fit 2). The overall fit is slightly better than the previous one.

If we extend the curve to the low-mass end ($\nu \lesssim 0.6$), both fits of Eqs. (A12) and (A13) somehow underestimate the ST mass function, but in this region the ST mass function tends to overpredict the true mass function of halos in the numerical simulations [65]. It might be also possible that low-mass halos are not described well by the simple model of Eq. (A2) in the first place, since the formation process of low-mass halos could be extremely stochastic and not be described well by the local values of the linear density field.

Finally, we comment on the difficulty in trying to analytically deconvolve the equations by using the Fourier transformation. The convolution integral is

formally solved by the Fourier transformation, and Eq. (A7) is given by

$$\Xi(x,\sigma) = \frac{1}{2}\int_{-\infty}^{\infty}\frac{dk}{2\pi}e^{-ikx/\sigma}\frac{\tilde{F}(k)}{\tilde{P}_\sigma(k/\sigma)}, \tag{A14}$$

where $\tilde{F}(k)$ and $\tilde{P}_\sigma(k)$ are the Fourier transforms of $F(\nu)$ and $P_\sigma(\delta)$, respectively. For a Gaussian distribution, we have $\tilde{P}_\sigma(k/\sigma) = e^{-k^2/2}$, and this integral converges only if $\tilde{F}(k)$ decays as fast as $e^{-k^2/2}$ for $k \to \infty$. Thus, the function $F(\nu)$ should be a sufficiently smooth function in the range of $-\infty < \nu < \infty$. Although the variable ν is a positive number, one can apply the analytic continuation to the function $F(\nu)$ for the negative values of ν.

The Fourier transform $\tilde{F}$ can be represented directly by a multiplicity function as

$$\tilde{F}(k) = \int_{-\infty}^{\infty} d\nu\left(\pi\delta_{\rm D}(k) + \frac{i}{k}e^{-ik\nu}\right)\frac{f(\nu)}{\nu}, \tag{A15}$$

where we assume the analytic continuation of the function $f(\nu)$ with negative argument $\nu < 0$ and use the fact that Fourier transform of the step function is given by a formula $\tilde{\Theta}(k) = \pi\delta_{\rm D}(k) - i/k$.

For the PS mass function with a Gaussian distribution, deconvolution with Eqs. (A14) and (A15) actually works. In fact, we have $f(\nu) = (2/\pi)^{1/2}\nu e^{-\nu^2/2}$ and $\tilde{F}(k) = 2\pi\delta_{\rm D}(k) + 2ie^{-k^2/2}/k$ in this case. Substituting the last expression and $\tilde{P}_\sigma(k/\sigma) = e^{-k^2/2}$ into Eq. (A14), we have $\Xi(x,\sigma) = \Theta(x)$, as expected.

In the ST mass function of Eq. (37), however, the integral of Eq. (A14) does not converge. The factor $f(\nu)/\nu$ is not regular at $\nu \to 0$ and scales as $\sim\nu^{-2p}$ near the origin. When $p > 0$, the derivative of $F(\nu)$ at the origin diverges. In the Fourier space, Eq. (A15) indicates that $\tilde{F}(k) \sim |k|^{2p-2}$ for large $|k|$, and the integral of Eq. (A14) does not converge for $\tilde{P}_\sigma(k/\sigma) \sim e^{-k^2/2}$. Thus, the convolution equation, Eq. (A7), does not have a regular solution when the function $f(\nu)/\nu$ is singular at $\nu = 0$, as in the case of ST mass function. The nonexistence of the solution in this case is more easily understood by Eq. (A8). According to this equation, we have $f(\nu)/\nu|_{\nu\to 0} = -2\sigma\int\Xi(\delta,\sigma)[\partial P_\sigma(\delta)/\partial\delta]d\delta$. The rhs of this equation is finite as long as the distribution function $P_\sigma(\delta)$ is a regular function and cannot reproduce the singularity of the lhs. This property is the reason why smooth models of Ξ, such as Eq. (A12), tend to underestimate the ST mass function extrapolated to the low-mass end.

APPENDIX B: ON THE CONNECTION BETWEEN PEAK THEORY AND THE iPT

In this Appendix, we highlight the connection that exists between the (Lagrangian) renormalized bias function in iPT [6,7] and the polynomial series expansion of Refs. [18,38]. Unlike in iPT, where the renormalized bias functions are defined independently of the statistical correlators under consideration, we shall start from the peak two-point correlation in Lagrangian space. Therefore, our conclusions formally apply to the two-point correlation only. However, we will argue below that it should also hold for higher-order correlation functions.

The Lagrangian, two-point correlation $\xi_{\rm pk}(r)$ of the density peaks can generically be written as

$$[1+\xi_{\rm pk}(r)]\bar{n}_{\rm pk}^2 = \int d^N y_1 d^N y_2 n_{\rm pk}(\boldsymbol{y}_1) n_{\rm pk}(\boldsymbol{y}_2) P(\boldsymbol{y}_1,\boldsymbol{y}_2;r), \tag{B1}$$

where $n_{\rm pk}(\boldsymbol{y})$ is the localized number density of the biased tracers (represented here as a set of constraints applied to the linear fluctuations fields $\boldsymbol{y}$), whereas $\bar{n}_{\rm pk}$ is the average number density.

We can write down the joint probablity distribution function (PDF) $P(\boldsymbol{y}_1,\boldsymbol{y}_2;r)$ as the Fourier transform

$$P(\boldsymbol{y}_1,\boldsymbol{y}_2;r) = \frac{1}{(2\pi)^{2N}}\int d^N J_1 d^N J_2 \exp\left(-\frac{1}{2}\boldsymbol{J}^\top\Sigma\boldsymbol{J}\right)e^{-i\boldsymbol{J}^\top\boldsymbol{y}}, \tag{B2}$$

where N is the dimension of $\boldsymbol{y}_i$ and, for shorthand convenience, we have $\boldsymbol{J} = (\boldsymbol{J}_1,\boldsymbol{J}_2)$ and $\boldsymbol{y} = (\boldsymbol{y}_1,\boldsymbol{y}_2)$. Moreover, $\Sigma \equiv (\boldsymbol{M},\boldsymbol{B}^\top;\boldsymbol{B},\boldsymbol{M})$ is the covariance matrix of $\boldsymbol{y}$. Substituting this relation into the definition of $\xi_{\rm pk}(r)$, we arrive at

$$1+\xi_{\rm pk}(r) = \prod_{a=1}^{2}\left(\frac{1}{(2\pi)^N\bar{n}_{\rm pk}}\int d^N J_a \tilde{n}_{\rm pk}(\boldsymbol{J}_a)e^{-(1/2)\boldsymbol{J}_a^\top\boldsymbol{M}\boldsymbol{J}_a}\right) \times\exp\left(-\boldsymbol{J}_1^\top\boldsymbol{B}^\top\boldsymbol{J}_2\right), \tag{B3}$$

where

$$\tilde{n}_{\rm pk}(\boldsymbol{J}_a) \equiv \int d^N y_a n_{\rm pk}(\boldsymbol{y}_a)e^{-i\boldsymbol{J}_a^\top\boldsymbol{y}_a} \tag{B4}$$

is the Fourier transform of the localized number density.

We will now expand $\exp(-\boldsymbol{J}_1^\top\boldsymbol{B}^\top\boldsymbol{J}_2)$ in series and exploit the fact that the covariance matrix $\boldsymbol{M}$ can be block diagonalized, i.e., $\boldsymbol{M} = {\rm diag}(\boldsymbol{M}_1,\ldots,\boldsymbol{M}_i,\ldots,\boldsymbol{M}_p)$. Let $\boldsymbol{J}_a = (\boldsymbol{J}_{a,1},\ldots,\boldsymbol{J}_{a,i},\ldots,\boldsymbol{J}_{a,p})$ be the corresponding decomposition of $\boldsymbol{J}_a$ in the frame in which $\boldsymbol{M}$ is diagonal (not necessarily unique block diagonal decomposition, but there is certainly a unique frame in which the number of blocks is maximal). Substituting the expression of $n_{\rm pk}(\boldsymbol{J})$, Eq. (B4), into Eq. (B3), we obtain

$$\begin{aligned}\xi_{\rm pk}(r) &= \frac{1}{[(2\pi)^N \bar{n}_{\rm pk}]^2}\int d^N J_1 \left\{\int d^N y_1 n_{\rm pk}(\boldsymbol{y}_1) e^{-i\boldsymbol{J}_1^\top \boldsymbol{y}_1}\right\} e^{-\frac{1}{2}\boldsymbol{J}_1^\top \boldsymbol{M}\boldsymbol{J}_1} \\ &\times \int d^N J_2 \left\{\int d^N y_2 n_{\rm pk}(\boldsymbol{y}_2) e^{-i\boldsymbol{J}_2^\top \boldsymbol{y}_2}\right\} e^{-\frac{1}{2}\boldsymbol{J}_2^\top \boldsymbol{M}\boldsymbol{J}_2} \left(\sum_{n=1}^{\infty} \frac{(-1)^n}{n!} (\boldsymbol{J}_1 \boldsymbol{B}^\top \boldsymbol{J}_2)^n\right) \\ &= \sum_{n=1}^{\infty} \frac{(-1)^n}{n!} \sum_{I_1, L_1=1}^{p} \cdots \sum_{I_n, L_n=1}^{p} \frac{1}{\bar{n}_{\rm pk}} \int d^N y_1 n_{\rm pk}(\boldsymbol{y}_1) \left\{\frac{1}{(2\pi)^N} \int d^N J_1 \boldsymbol{J}_{1,I_1}^\top \times \cdots \times \boldsymbol{J}_{1,I_n}^\top e^{-\frac{1}{2}\boldsymbol{J}_1^\top \boldsymbol{M}\boldsymbol{J}_1} e^{-i\boldsymbol{J}_1^\top \boldsymbol{y}_1}\right\} \boldsymbol{B}_{I_1 L_1}^\top \\ &\times \cdots \times \boldsymbol{B}_{I_n L_n}^\top \times \frac{1}{\bar{n}_{\rm pk}} \int d^N y_2 n_{\rm pk}(\boldsymbol{y}_2) \left\{\frac{1}{(2\pi)^N} \int d^N J_2 \boldsymbol{J}_{2,L_1} \times \cdots \times \boldsymbol{J}_{2,L_n} e^{-\frac{1}{2}\boldsymbol{J}_2^\top \boldsymbol{M}\boldsymbol{J}_2} e^{-i\boldsymbol{J}_2^\top \boldsymbol{y}_2}\right\} \\ &= \sum_{n=1}^{\infty} \frac{(-1)^n}{n!} \sum_{I_1, L_1=1}^{p} \cdots \sum_{I_n, L_n=1}^{p} \left\{\frac{1}{\bar{n}_{\rm pk}} \int d^N y_1 n_{\rm pk}(\boldsymbol{y}_1) i^n \frac{\partial^\top}{\partial \boldsymbol{y}_{1,I_1}} \cdots \frac{\partial^\top}{\partial \boldsymbol{y}_{1,I_n}} P(\boldsymbol{y}_1)\right\} \boldsymbol{B}_{I_1 L_1}^\top \times \cdots \times \boldsymbol{B}_{I_n L_n}^\top \\ &\times \left\{\frac{1}{\bar{n}_{\rm pk}} \int d^N y_2 n_{\rm pk}(\boldsymbol{y}_2) i^n \frac{\partial}{\partial \boldsymbol{y}_{2,L_1}} \cdots \frac{\partial}{\partial \boldsymbol{y}_{2,L_n}} P(\boldsymbol{y}_2)\right\}. \end{aligned} \tag{B5}$$

Here, I_α (respectively, L_α) designates the subsets of variables $\boldsymbol{y}_{1,I_\alpha} \in \boldsymbol{y}_1$ (respectively, $\boldsymbol{y}_{2,L_\alpha} \in \boldsymbol{y}_2$) that correlate *at a given spatial location*. The block diagonalization implies that we have $p \leq N$ such subsets. Through a suitable change of variables, we can also write $\boldsymbol{y}_{1,I_\alpha}$ in the form $\boldsymbol{y}_{1,I_\alpha} = (\boldsymbol{w}_{I_\alpha}, \Omega_{I_\alpha})$, where Ω_{I_α} are angles which we want to integrate out. For illustration, in the case of the peak constraint for which $\boldsymbol{y}_1 = \{\nu, \eta_i, \zeta_{ij}\}$, we can split $\boldsymbol{y}_1$ into three subsets, $\boldsymbol{y}_1 = (\boldsymbol{y}_{1,I=1}, \boldsymbol{y}_{1,I=2}, \boldsymbol{y}_{1,I=3})$ such that

$$\boldsymbol{y}_{1,I=1} = \{\nu, J_1\} \tag{B6}$$

$$\boldsymbol{y}_{1,I=2} = \{\eta_1, \eta_2, \eta_3\} = \{\eta^2, 2\,\text{angles}\} \tag{B7}$$

$$\boldsymbol{y}_{1,I=3} = \{\tilde{\zeta}_{ij}\} = \{J_2, J_3, 3\,\text{angles}\}, \tag{B8}$$

where $\tilde{\zeta}_{ij}$ are the five independent components of the Hessian; the two angles in $\boldsymbol{y}_{1,2}$ and the three angles in $\boldsymbol{y}_{1,3}$ describe the orientation of the vector $\boldsymbol{\eta}$ and the principal axis frame of the tensor $\tilde{\zeta}_{ij}$, respectively; and the invariants J_i are defined in Ref. [18].

Furthermore, the cross-covariance matrix $\boldsymbol{B}_{IL}^\top$ is of the form

$$\boldsymbol{B}_{IL}^\top = \int \frac{d^3k}{(2\pi)^3} \boldsymbol{U}_I(-\boldsymbol{k}) \boldsymbol{U}_L^\top(\boldsymbol{k}) P_{\rm L}(k) e^{i\boldsymbol{k}\cdot\boldsymbol{r}}, \tag{B9}$$

where $\delta(\boldsymbol{k})$ are the Fourier mode of the *unsmoothed* linear density field, $P_0(k)$ is its power spectrum, and $\boldsymbol{U}_I(\boldsymbol{k})$ are functions of the wave number analogous to those introduced in Eq. (22). For instance,

$$\boldsymbol{U}_{I=1}(\boldsymbol{k}) = \left(\frac{1}{\sigma_0}, \frac{k^2}{\sigma_2}\right) W_s(kR_s) \tag{B10}$$

for the peak height ν and curvature J_1, and

$$\boldsymbol{U}_{I=2}(\boldsymbol{k}) = \frac{i}{\sigma_1}(k_1, k_2, k_3) W_s(kR_s) \tag{B11}$$

for $\boldsymbol{y}_{1,2}$ corresponding to the vector components η_i, whereas

$$\boldsymbol{U}_{I=3}(\boldsymbol{k}) = \frac{1}{\sigma_2}\left(-k_1^2 + \frac{k^2}{3}, -k_2^2 + \frac{k^2}{3}, -k_3^2 + \frac{k^2}{3}, -k_1 k_2, -k_1 k_3, -k_2 k_3\right) W_s(kR_s) \tag{B12}$$

for the components $\tilde{\zeta}_{ij}$ of the traceless matrix. Here, $k^2 = k_1^2 + k_2^2 + k_3^2$, and $W_s(kR_s)$ is the Fourier transform of the filtering kernel. We use the same notation as Ref. [6] to emphasize that we are talking about the same quantity.

Substituting this relation into the expression of $\xi_{\rm pk}(r)$, we obtain

$$\begin{aligned}\xi_{\rm pk}(r) = &\sum_{n=1}^{\infty}\frac{1}{n!}\sum_{I_1,L_1=1}^{p}\cdots\sum_{I_n,L_n=1}^{p}\int\frac{d^3k_1}{(2\pi)^3}\cdots\int\frac{d^3k_n}{(2\pi)^3}\\ &\times\left\{\frac{1}{\bar{n}_{\rm pk}}\int d^N y_1 n_{\rm pk}(\boldsymbol{y}_1)\frac{\partial^\top}{\partial\boldsymbol{y}_{1,I_1}}\boldsymbol{U}_{I_1}(-\boldsymbol{k}_1)\cdots\frac{\partial^\top}{\partial\boldsymbol{y}_{1,I_n}}\boldsymbol{U}_{I_n}(-\boldsymbol{k}_n)P(\boldsymbol{y}_1)\right\}\\ &\times\left\{\frac{1}{\bar{n}_{\rm pk}}\int d^N y_2 n_{\rm pk}(\boldsymbol{y}_2)\boldsymbol{U}^\top_{L_1}(\boldsymbol{k}_1)\frac{\partial}{\partial\boldsymbol{y}_{2,L_1}}\cdots\boldsymbol{U}^\top_{L_n}(\boldsymbol{k}_n)\frac{\partial}{\partial\boldsymbol{y}_{2,L_n}}P(\boldsymbol{y}_2)\right\}\\ &\times P_{\rm L}(k_1)\ldots P_{\rm L}(k_n)e^{i(\boldsymbol{k}_1+\cdots+\boldsymbol{k}_n)\cdot\boldsymbol{r}}.\end{aligned}\tag{B13}$$

It is not difficult to see that the partial derivatives with respect to the variables $\boldsymbol{y}_{1,I}$ and $\boldsymbol{y}_{2,L}$ correspond to the renormalized bias functions of iPT. Namely, we have

$$c^L_n(\boldsymbol{k}_1,\ldots,\boldsymbol{k}_n)\equiv\sum_{I_1,\ldots,I_n=1}^{p}\left\{\frac{1}{\bar{n}_{\rm pk}}\int d^N y n_{\rm pk}(\boldsymbol{y})\boldsymbol{U}^\top_{I_1}(\boldsymbol{k}_1)\frac{\partial}{\partial\boldsymbol{y}_{I_1}}\cdots\boldsymbol{U}^\top_{I_n}(\boldsymbol{k}_n)\frac{\partial}{\partial\boldsymbol{y}_{I_n}}P(\boldsymbol{y})\right\}.\tag{B14}$$

For example, considering only the variables relevant to a peak constraint and on writing $P(\boldsymbol{y})=\prod_I P(\boldsymbol{y}_I)=P(\boldsymbol{w})P(\Omega_\eta,\Omega_{\tilde{\zeta}})$, where Ω_η and $\Omega_{\tilde{\zeta}}$ are the angles associated with $\boldsymbol{\eta}$ and $\tilde{\zeta}_{ij}$ and $\boldsymbol{w}=(\nu,J_1,3\eta^2,5J_2,J_3)$, we find that the linear renormalized bias function is

$$\begin{aligned}&\sum_{I=1}^{p}\frac{1}{\bar{n}_{\rm pk}}\int d^N y n_{\rm pk}(\boldsymbol{y})\boldsymbol{U}^\top_I(\boldsymbol{k})\frac{\partial}{\partial\boldsymbol{y}_I}P(\boldsymbol{y})\\ &\quad=\frac{1}{\bar{n}_{\rm pk}}\int d^N y n_{\rm pk}(\boldsymbol{y})P(\boldsymbol{y})\sum_{I=1}^{p}\left(P(\boldsymbol{y}_I)^{-1}\boldsymbol{U}^\top_I(\boldsymbol{k})\frac{\partial}{\partial\boldsymbol{y}_I}P(\boldsymbol{y}_I)\right)\\ &\quad=\frac{1}{\bar{n}_{\rm pk}}\int d\boldsymbol{w} n_{\rm pk}(\boldsymbol{w})P(\boldsymbol{w})\left\{\mathcal{N}(\nu,J_1)^{-1}\frac{1}{\sigma_0}\left(\frac{\partial}{\partial\nu}+\frac{k^2}{\sigma_2}\frac{\partial}{\partial J_1}\right)\mathcal{N}(\nu,J_1)\right.\\ &\qquad\left.+\int\Omega_\eta e^{3\eta^2/2}\frac{i}{\sigma_1}\sum_i k_i\frac{\partial}{\partial\eta_i}e^{-3\eta^2/2}+\int\Omega_{\tilde{\zeta}}e^{5J_2/2}\frac{1}{\sigma_2}\sum_{i\le j}\left(-k_ik_j+\frac{1}{3}\delta_{ij}k^2\right)\frac{\partial}{\partial\tilde{\zeta}_{ij}}e^{-5J_2/2}\right\}W_s(kR_s)\\ &\quad\equiv(b_{10}+b_{01}k^2)W_s(kR_s),\end{aligned}$$

which coincides indeed with the linear bias of peaks. We have exploited the fact that the localized peak number density depends only on the variables $\boldsymbol{w}$ to average the derivative operators over the angular variables $(\Omega_\eta,\Omega_{\tilde{\zeta}})$. This way, we follow the same logic as Ref. [18] and our discussion in Sec. III. We have also checked that the agreement also holds at second order, though the calculation is already much more involved.

Therefore, this clearly suggests that the peak two-point correlation $\xi_{\rm pk}(r)$ can also be written as

$$\xi_{\rm pk}(r)=\sum_{n=1}^{\infty}\frac{1}{n!}\int\frac{d^3k_1}{(2\pi)^3}\ldots\int\frac{d^3k_n}{(2\pi)^3}[c^{(n)}_X(\boldsymbol{k}_1,\ldots,\boldsymbol{k}_n)]^2P_{\rm L}(k_1)\cdots P_{\rm L}(k_n)e^{i(\boldsymbol{k}_1+\cdots+\boldsymbol{k}_n)\cdot\boldsymbol{r}},\tag{B15}$$

which agrees with the iPT result in the absence of gravitationally induced motions.

[1] M. Davis, G. Efstathiou, C. S. Frenk, and S. D. M. White, Astrophys. J. **292**, 371 (1985).
[2] N. Kaiser, Astrophys. J. Lett. **284**, L9 (1984).
[3] N. Kaiser, Mon. Not. R. Astron. Soc. **227**, 1 (1987).
[4] A. J. S. Hamilton, Astrophys. J. Lett. **385**, L5 (1992).
[5] F. Bernardeau, S. Colombi, E. Gaztañaga, and R. Scoccimarro, Phys. Rep. **367**, 1 (2002).
[6] T. Matsubara, Phys. Rev. D **83**, 083518 (2011).
[7] T. Matsubara, Phys. Rev. D **90**, 043537 (2014).
[8] N. Dalal, O. Doré, D. Huterer, and A. Shirokov, Phys. Rev. D **77**, 123514 (2008).
[9] T. Buchert, Astron. Astrophys. **223**, 9 (1989).
[10] F. Moutarde, J.-M. Alimi, F. R. Bouchet, R. Pellat, and A. Ramani, Astrophys. J. **382**, 377 (1991).
[11] T. Buchert, Mon. Not. R. Astron. Soc. **254**, 729 (1992).
[12] P. Catelan, Mon. Not. R. Astron. Soc. **276**, 115 (1995); R. Juszkiewicz, Astron. Astrophys. **298**, 643 (1995).
[13] S. Bharadwaj, Astrophys. J. **472**, 1 (1996).
[14] P. Catelan, F. Lucchin, S. Matarrese, and C. Porciani, Mon. Not. R. Astron. Soc. **297**, 692 (1998).
[15] C. Porciani, S. Matarrese, F. Lucchin, and P. Catelan, Mon. Not. R. Astron. Soc. **298**, 1097 (1998).
[16] C. Rampf and T. Buchert, J. Cosmol. Astropart. Phys. 6 (2012) 021.
[17] J. M. Bardeen, J. R. Bond, N. Kaiser, and A. S. Szalay, Astrophys. J. **304**, 15 (1986).
[18] T. Lazeyras, M. Musso, and V. Desjacques, Phys. Rev. D **93**, 063007 (2016).
[19] J. R. Bond and S. T. Myers, Astrophys. J. Suppl. Ser. **103**, 1 (1996).
[20] Y. Ohta, I. Kayo, and A. Taruya, Astrophys. J. **608**, 647 (2004).
[21] R. K. Sheth, K. C. Chan, and R. Scoccimarro, Phys. Rev. D **87**, 083002 (2013).
[22] H. J. Mo and S. D. M. White, Mon. Not. R. Astron. Soc. **282**, 347 (1996).
[23] H. J. Mo, Y. P. Jing, and S. D. M. White, Mon. Not. R. Astron. Soc. **284**, 189 (1997).
[24] L. Appel and B. J. T. Jones, Mon. Not. R. Astron. Soc. **245**, 522 (1990).
[25] A. Paranjape and R. K. Sheth, Mon. Not. R. Astron. Soc. **426**, 2789 (2012).
[26] V. Desjacques, Phys. Rev. D **78**, 103503 (2008).
[27] V. Desjacques, M. Crocce, R. Scoccimarro, and R. K. Sheth, Phys. Rev. D**82**, 103529 (2010).
[28] T. Matsubara, Phys. Rev. D **77**, 063530 (2008).
[29] T. Matsubara, Phys. Rev. D **92**, 023534 (2015).
[30] T. Matsubara, Phys. Rev. D **86**, 063518 (2012).
[31] K. C. Chan, R. K. Sheth, and R. Scoccimarro, arXiv: 1511.01909.
[32] D. Pogosyan, C. Gay, and C. Pichon, Phys. Rev. D **80**, 081301 (2009); **81**, 129901(E) (2010).
[33] C. Gay, C. Pichon, and D. Pogosyan, Phys. Rev. D **85**, 023011 (2012).
[34] V. Desjacques, J.-O. Gong, and A. Riotto, J. Cosmol. Astropart. Phys. 09 (2013) 006.
[35] W. H. Press and P. Schechter, Astrophys. J. **187**, 425 (1974).
[36] R. K. Sheth and G. Tormen, Mon. Not. R. Astron. Soc. **308**, 119 (1999).
[37] A. G. Doroshkevich, Astrofiz. **6**, 581 (1970).
[38] V. Desjacques, Phys. Rev. D **87**, 043505 (2013).
[39] M. Biagetti, K. C. Chan, V. Desjacques, and A. Paranjape, Mon. Not. R. Astron. Soc. **441**, 1457 (2014).
[40] A. Paranjape, R. K. Sheth, and V. Desjacques, Mon. Not. R. Astron. Soc. **431**, 1503 (2013).
[41] A. M. Dizgah, K. C. Chan, J. Noreña, M. Biagetti, and V. Desjacques, arXiv:1512.06084.
[42] Planck Collaboration, arXiv:1502.01589.
[43] T. Baldauf, V. Desjacques, and U. Seljak, Phys. Rev. D **92**, 123507 (2015).
[44] M. Davis, G. Efstathiou, C. S. Frenk, and S. D. M. White, Astrophys. J. **292**, 371 (1985).
[45] C. Lacey and S. Cole, Mon. Not. R. Astron. Soc. **271**, 676 (1994).
[46] D. J. Eisenstein and W. Hu, Astrophys. J. **511**, 5 (1999).
[47] J. Carlson, B. Reid, and M. White, Mon. Not. R. Astron. Soc. **429**, 1674 (2013).
[48] M. Sato and T. Matsubara, Phys. Rev. D **84**, 043501 (2011).
[49] M. Sato and T. Matsubara, Phys. Rev. D **87**, 123523 (2013).
[50] T. Matsubara, Phys. Rev. D **78**, 083519 (2008).
[51] L. Guzzo *et al.*, Nature (London) **451**, 541 (2008).
[52] T. Okumura *et al.*, Publ. Astron. Soc. Jpn. **68**, 38 (2016).
[53] S. Matarrese and L. Verde, Astrophys. J. Lett. **677**, L77 (2008).
[54] A. Slosar, C. Hirata, U. Seljak, S. Ho, and N. Padmanabhan, J. Cosmol. Astropart. Phys. 08 (2008) 031.
[55] Planck Collaboration, arXiv:1502.01592.
[56] M. Biagetti and V. Desjacques, Mon. Not. R. Astron. Soc. **451**, 3643 (2015).
[57] V. Desjacques, U. Seljak, and I. T. Iliev, Mon. Not. R. Astron. Soc. **396**, 85 (2009).
[58] V. Desjacques and R. K. Sheth, Phys. Rev. D **81**, 023526 (2010).
[59] , Y. Zheng, P. Zhang, and Y. Jing, Phys. Rev. D **91**, 123512 (2015).
[60] A. Elia, A. D. Ludlow, and C. Porciani, Mon. Not. R. Astron. Soc. **421**, 3472 (2012).
[61] A. Paranjape, T. Y. Lam, and R. K. Sheth, Mon. Not. R. Astron. Soc. **420**, 1429 (2012).
[62] M. Biagetti, K. C. Chan, V. Desjacques, and A. Paranjape, Mon. Not. R. Astron. Soc. **441**, 1457 (2014).
[63] W. H. Richardson, J. Opt. Soc. Am. **62**, 55 (1972).
[64] L. B. Lucy, Astron. J. **79**, 745 (1974).
[65] A. A. Klypin, S. Trujillo-Gomez, and J. Primack, Astrophys. J. **740**, 102 (2011).